Master's Dissertation
Common Mode Effect of the ALICE Transition Radiation Detector - Baseline Shift

University of Cape Town

Ali Elimam
ELMALI001
Supervisor: Dr. Thomas Dietel

January 21, 2021

Submitted to the Department of Electrical Engineering in partial fulfilment of the requirements for the Master of Engineering specialising in Nuclear Power degree.

Abstract

Common Mode Effect of the ALICE Transition Radiation Detector - Baseline Shift.

The Transition Radiation Detector is a sub-detector of the ALICE experiment that is used primarily as an electron detector and a trigger mechanism. The TRD currently has 521 individual chambers distributed over 18 super modules. Each chamber houses a radiator, a drift region and a multi-wire proportional chamber with the readout electronics. When charge is absorbed in the anode wires of the multi-wire proportional chamber, it creates a common-mode effect, this common-mode effect manifests itself as a drop in the signal produced by the surrounding readout electronics where no particle has traversed, called the baseline. Capacitors have been installed in a layout to produce a low-pass filter (RC circuit) to decrease the impact of the common-mode effect. These capacitors were installed for a pad row pair, creating capacitor coupling for a high voltage supply segment. However, these capacitors were prone to failure, causing dead chambers that could not be used to acquire data for the remainder of the run, so it was decided to remove them. With their removal, the extent of the common-mode effect on the baseline had to be understood and corrected for in order to better calibrate the detector system. The University of Cape Town has one chamber, an L3C0 chamber. This chamber was used to collect two datasets with the same parameters, one with the 2.2 nF capacitors installed and the other without the 2.2 nF capacitors, to study the effect. It is found that the drop in baseline is only experienced by anode wires with the same capacitor coupling. Furthermore, it is observed that there is a linear relationship between the charge absorbed by the anode wires and the drop in baseline, thus charge absorbed by the anode wires can be summed should they have the same capacitor coupling. It is also found that the drop in baseline is 2.5 times larger in the dataset without capacitors. The final part of the thesis corrects for this common-mode effect, using a correction factor determined from the dataset.

Contents

List of Figures

List of Tables

Chapter 1

Introduction

Where did we come from? How did everything in existence today come to be? Where did it all begin?

The most known, and most accepted theory at this time, is the *Big Bang* theory, coined by scientist Georges Lemaitre in the early 20^{th} century [20]. Lemaitre stated that the universe could be traced back to a single point origin, in this case, called the *primeval atom*, this statement was supported by Edwin Hubble through the observation of the interstellar red shifts, where galaxies are seen to be drifting further away from each other, in every direction.

CERN is the world leading organisation in the realm of nuclear and particle research, as well as how these particles come together to form complex macro systems. It functions by accelerating and colliding nuclei and subatomic particles at near the speed of light and studying the resulting phenomenon. CERN attempts to answer some of the questions asked concerning the universe. This is done with the *Large Hadron Collider* (LHC) and multiple detectors. Scientists and researchers from across the globe gather together to collaborate on projects that constantly push the bounds of humanity on the knowledge and understanding of the universe. Research ranging from the quantum chromodynamics and super-symmetry, to searching for extra dimensions and dark matter is conducted.

One of the detectors used is the *ALICE* detector, ALICE is an acronym for *A Large Ion Collider Experiment*. The ALICE detector is used to research the *Quark Gluon Plasma*, or QGP, a state of matter under near unreasonable temperatures where quarks and gluons are free, a state that is believed to be in existence up to 10 µs after the big bang. [10]

Within the ALICE detector is a number of sub-detectors, one sub-detector system is the *Transition Radiation Detector*, or TRD, which functions as the main electron detector in the collisions that take place within the LHC. The TRD itself is made of 18 super-modules, each super-module housing up to 30 individual readout chambers.

When a readout chamber detects a particle and produces a signal, it affects the surroundings within the chamber, causing a drop in the signal produced within these surroundings, this drop in signal produced is termed the *Baseline Shift*. The notion of a particle traversing the chamber and the surroundings at the point of traversal being affected is called the *Common-Mode effect*. Thus the ALICE TRD uses capacitors for regulation, to minimise

this effect.

An issue that arises is that these capacitors are prone to failure within the TRD of the ALICE detector, where it then produces dead chambers that cannot be used to acquire data for the remainder of the run. At the end of run 2 of ALICE, a total of 83 chambers were faulty, of which 76 were fixed by the removal of capacitors (91%)[11]. Hence, the solution of their removal, which has been done in preparation for run 3, the next collision cycle at CERN scheduled for 2021. Thus, understanding the effects of removing the capacitors becomes paramount in order to be able to correct for it. This thesis focuses on understanding these effects.

The attempt to understand the effects of removal of the capacitors is done using the TRD readout chamber at the University of Cape Town. This is done by setting a controlled environment and using the detector chamber to acquire data with all the variables constant, the key difference being one data set is acquired with capacitors installed and the other without capacitors. Both data sets are analysed to determine the baseline shift due to detected particle traversal and the extent of the common mode effect.

The ALICE detector is currently undergoing a massive upgrade, to the O^2 (Online-Offline) software, in preparation for the next run of experimental collisions to collect data, *run* 3. The results of this thesis are intended for implementation within this software framework for the next run.

Chapter 2

Particles and Detectors

2.1 Theoretical Background

2.1.1 The Standard Model

Atoms form the basic composition of all known and understood matter, where each atom is made of protons and neutrons within the nucleus, along with the orbiting electrons. The protons and neutrons are in turn made of quarks bound together by gluons. Quarks have yet to be observed in isolation, but they and gluons are permanently bound inside the composite sub-atomic particles, this is known as confinement [3].

The *Standard Model* has been successfully examined to a high degree of accuracy to best describe the fundamentals of particle physics, see figure 2.1 below. Particles in the standard model are set and differentiated through three different characteristics, their *mass, spin* and *charge*. *Fermions*, are characterised by their spin of 1/2 and separated into three families, each containing the same charge but different masses, the heavier fermion family, family 3, is unstable and when created in nature and rapidly decays into the lighter fermions, which in turn make up most of the matter, including life. The fermions in a family are discernible from each other by their varying charges.

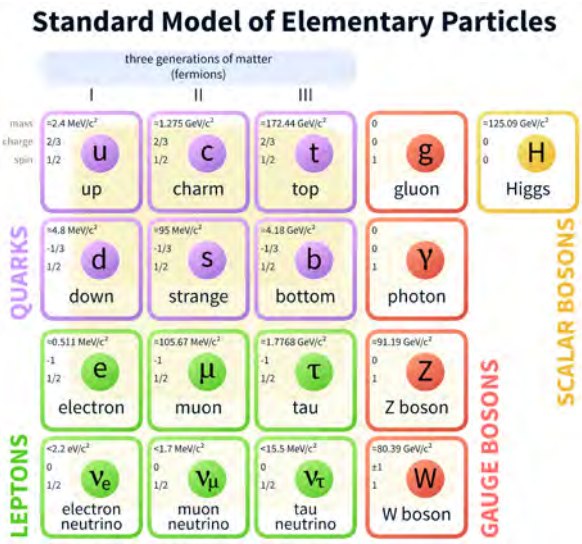

Figure 2.1: The Standard Model of Particle Physics

There are 2 quarks, *up* and *down*, which have electromagnetic charges of 2/3 and -1/3

respectively, quarks are the inherent ingredients to the hadrons, of which protons and neutrons are a part, where a proton has 2 up and 1 down quarks and a neutron has 2 down and one up quarks, thus giving them their +1 and 0 charges respectively. Mesons, such as the π^0 and η-mesons, are built from a quark anti-quark pair. There are also 2 leptons with charges of -1 and 0, which correspond to the down and up leptons, commonly given the names of electrons and neutrinos respectively.

The interactions within the standard model are linked to three vector *bosons*, with a spin of 1, each boson mediating the interactions. Gluons mediate the strong interactions within atomic nuclei, photons mediate the electromagnetic interactions, while Z and W bosons (together called the intermediate vector bosons) mediate the weak interactions. Gluons and photons are massless, while Z and W are massive, which leads to evidence as to why weak interactions are weak at low energies, since their forces are suppressed by $E/M_{Z,W}$, however, this is only true for low energies [3].

2.1.2 Quantum Chromodynamics and Quark Gluon Plasma

Quantum Chromodynamics, QCD, is a theory of the strong interactions between quarks and gluons within hadrons, describing their interactions through their quantum numbers. The theory was born through a generalisation of *quantum electrodynamics*, (QED), the theory describing how light and matter interact. The main difference is with their gauge bosons, where as the photons of QED do not transfer charge, the gluons of QCD are not neutral and thus produce important characteristics in QCD, these characteristics are outside the scope of this thesis but more can be found on [10].

Under extremely high temperatures, the sub-atomic particles/hadrons break down and produce a *quark gluon plasma*, or QGP, a state of free quarks and gluons. The current belief is that in the early life of the universe, up to 10 µs after the big bang, the universe consisted of all the matter, all the anti-matter and all the energy of today. At about 1 µs, the neutrinos decouple and the universe creates subatomic particles, including protons and neutrons. At 2 minutes, nucleo-synthesis begins, where the composite elements of the universe fuse to form heavier elements, including α particles (Helium nuclei). At and beyond 20 minutes after the big bang, the universe is no longer hot enough for fusion of nuclei due to expansion and cooling, however, it is still hot and dense enough to restrict stability of nuclei [4]. Thus, studying the QGP may lead to insights at the near birth of the universe.

2.1.3 Bethe-Bloch Formula

When a charged particle traverses a medium and interacts with matter, it excites and ionises the atoms within the medium. The Bethe formula describes the mean energy loss over a distance travelled by the charged particles in the medium [8]. Hans Bethe released two different equations, one for relativistic particles and the other for non relativistic particles, here, only the relativistic version is considered.
For a particle of velocity v, charge z and energy E travelling a distance x into a medium of electron density n and excitation potential I, the mean energy loss of the particle across the medium per unit distance is:

$$-\left\langle \frac{dE}{dx} \right\rangle = 4\pi N_a r_e^2 m_e c^2 \frac{Z}{A}\frac{z^2}{\beta^2}\left[ln\left(\frac{2m_e c^2 \beta^2 \gamma^2 T_{max}}{I^2}\right) - \beta^2 - \frac{\delta(\beta\gamma)}{2}\right] \quad [8] \tag{2.1}$$

where c is the speed of light, $\beta = \frac{v}{c}$, r_e and m_e are the electron radius and mass respectively, A is the atomic mass of the medium and T_{max} is the maximum transferable energy to a single photon in a collision. For particles with high kinetic energies (relativistic particles), the radiative mechanism of energy loss is important to understanding the way the energy is released, these can be pair production, bremsstrahlung interactions or photonuclear interactions [4]. See figure 2.2.

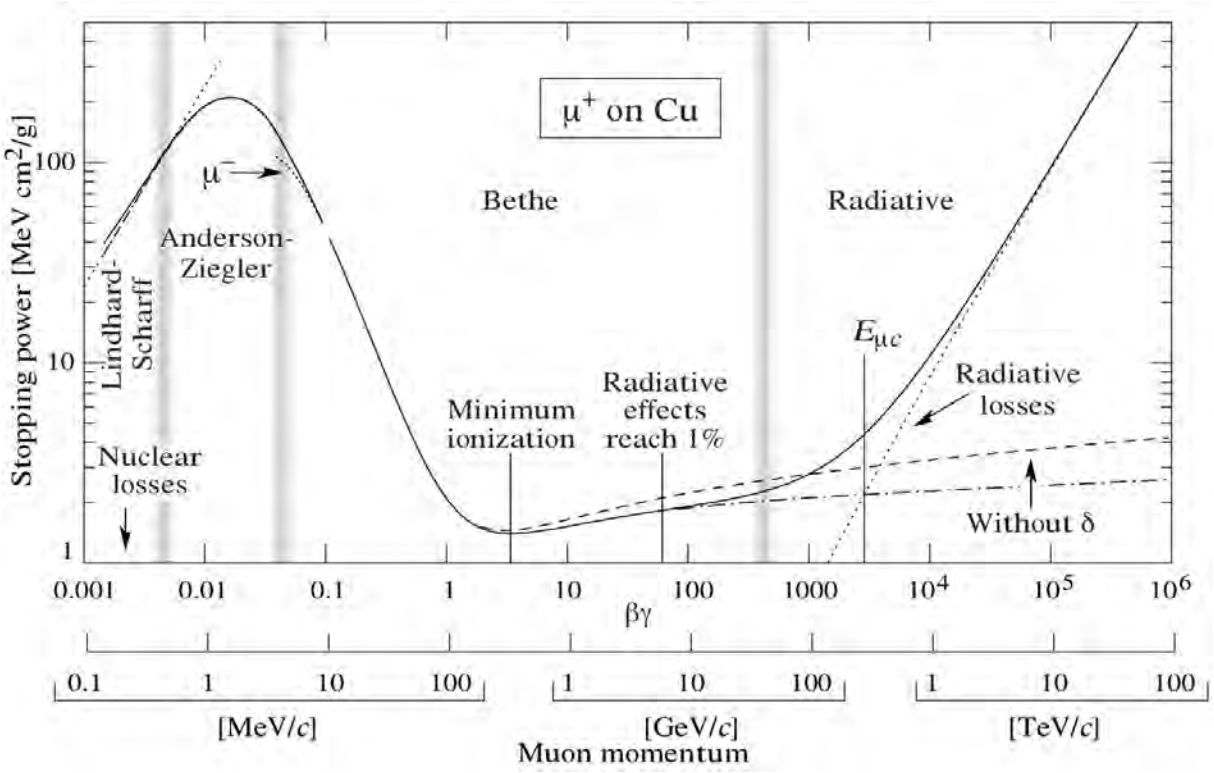

Figure 2.2: The Bethe curve of a muon in copper, giving the mean rate of energy loss as a function of momentum [4].

2.2 Proportional Counters and Drift Chambers

2.2.1 Proportional Counters

A proportional counter is, as the name suggests, a counter whose signals are proportional to the amount of charge absorbed. When a particle traverses the chamber of the proportional counter, it ionises the gas housed between these electrodes, this ionisation liberates positively charged ions and negatively charged electrons. If a strong electric field (in the form of a potential difference) is applied across these electrodes, upon liberation of the electron and ions, the electrons drift to the anode, while the ions drift to the cathode. As the electrons reach close proximity to the anode wire, an avalanche occurs, where there is an exponential rise in the number of particles as they are accelerated towards the anode. This exponential increase in electron numbers is related to the potential difference and called the gain proportionality. These electrons are then picked up and reflect as the signal. At certain voltages, however, the signal output plateaus and the same signal is produced regardless of an increase in the potential difference across the plates, this voltage above which there is no further increase in signal produced is called the saturation volt-

age, leading to a saturated gain, where the same signal is detected regardless of the initial ionising event [2]. In these cases, the maximum gain that can be achieved before reaching saturation is dependent on the gas used. Figure 2.3 below gives a time representation of the avalanche effect.

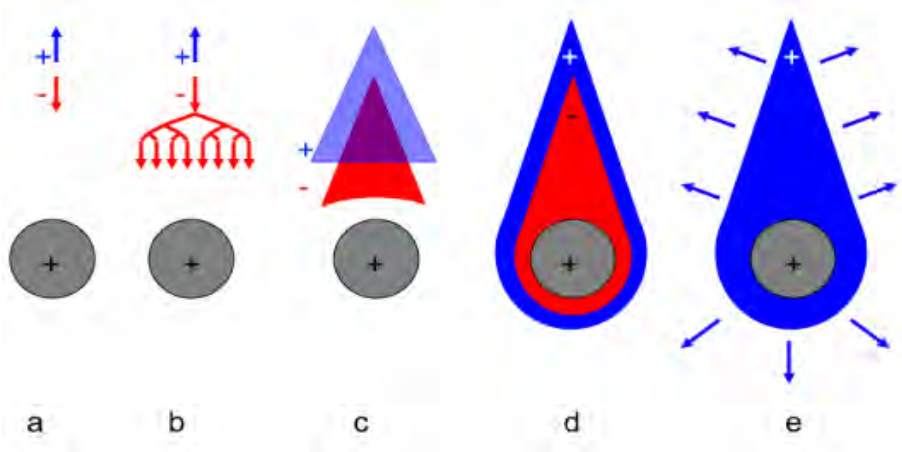

Figure 2.3: Development of an avalanche close to the anode wire, where the red signifies the electrons and blue the ions. a) shows the initial interaction and drift, b) the separation and initial amplification, c) close to the anode wire, a large number of electrons with accompanying ions is produced, d) the drop-like effect of the electrons surrounding the wire, e) upon absorption of electrons, the ions are repelled by the anode wire [4].

Proportional counters maintain the information of the particle that traversed based on proportionality, to a limit, through a multiplication factor. Considering the exponential rise in the number of electrons as they approach the anode wide, the multiplication factor M is given by [2] as:

$$M = \exp\left[2\sqrt{\frac{KNCV_0 a}{2\pi\epsilon_0}}\left(\sqrt{\frac{V_0}{V_T}} - 1\right)\right] \tag{2.2}$$

where C is the capacitance, V_0 and V_T are the potential difference and threshold voltage respectively, a is the radius of the anode wire, N is the number of molecules per unit volume, ϵ_0 is the dielectric constant and K is a specific gas property relating to the the threshold of multiplication and is given as $1.81 \times 10^{-17}\text{cm}^2\ \text{V}^{-1}$ for Argon gas [2].

The avalanche effect only begins within 50 µm of the anode wire, meaning most avalanches both start and end over the span of a nanosecond, where after absorption of the electrons, the ions drift towards the cathode wires. The charge absorbed along both wires, is then the detected signal. A large amount of electrons produced during the avalanche effect are created just before the last mean free path, which is the average distance an electron traverses in a medium before interacting with another particle, making electron contributions to the detected signal small. The positive ions that drift across to the cathode wires contribute significantly to the signal [2]. The ratio of contribution of charge is determined as:

$$\frac{v^-}{v^+} = \frac{ln(a+\lambda) - ln(a)}{ln(b) - ln(a+\lambda)} \quad [2] \tag{2.3}$$

where v^- and v^+ are the electron and ion contributions respectively, a is the wire radius, b is the cathode radius and λ is the initial distance at which charge is created. The above equation shows that, for average proportional counters, the average contribution

of electrons to the signal is 1% [2]. Following the above with the electron contribution to the detected signal neglected, Sauli [2] determined the drift time of the ions to be given by:

$$T = \frac{\pi\epsilon_0 P(b^2 - a^2)}{\mu^+ C V_0} \quad [2] \tag{2.4}$$

where P is the pressure of the gas in the chamber and μ^+ is the mobility of ions. For a typical chamber operating at $V_0 = 3000$ V, capacitance C = 8 pF/m and standard wire geometry of a = 10 µm and b = 8 mm, the drift time is T = 550 µs. Sauli [2] has also determined the signal induced on the anode wire can be given as:

$$v(t) = -\int_0^t dv = -\frac{Q}{2\pi\epsilon_0 l} ln \frac{r(t)}{a} \quad [2] \tag{2.5}$$

Substituting in the same variables used in equation 2.4, we see that 68% of the signal is produced in 700 ns, which means it is produced in 1/785 of the total time. Thus, a resistor is installed to control the rate of charging and discharging of the capacitor, such that the signal is differentiated with a time constant $\tau = RC$, making an RC circuit represented in figure 2.4.

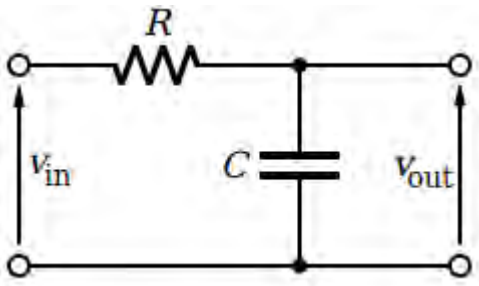

Figure 2.4: A circuit drawing of a simple low-pass filter.

Short pulses can then be obtained using low impedance terminations with the benefit of increasing the rate capability of the counter. Since the capacitors act as a voltage regulator to smooth out a DC power supply, this produces a voltage roughly proportional to the count rate. The removal of the capacitors would cause fluctuations in the voltage supply. A deeper explanation, with relation to this thesis is give in section 3.6.

2.2.2 Multi-Wire Proportional Chambers

Though proportional chambers are still widely used, they have a specific subset of limitations, primarily the signal output time for high frequency environments is relatively long, and spatial localisation, which is limited to only determining if a particle has traversed the detector, but not where in the detector. A multi-wire proportional chamber (MWPC) is essentially a proportional counter but with multiple anode wires spaced equally from one another, all with the same potential in between two cathode planes, hence, each wire acting as its own counter [2]. The accuracy of localisation is dependent on the wire spacing, spaces less than 2 mm become challenging to operate due to proximity with other wires.

The capacitance of a general MWPC is determined through standard electrostatic equations, where it has been determined to be:

$$C = \frac{2\pi\epsilon_0}{(\pi l/s) - ln(2\pi a/s)} \quad [2] \tag{2.6}$$

where a is the wire radius, l is the distance to the cathode plane and s is the distance between the wires.

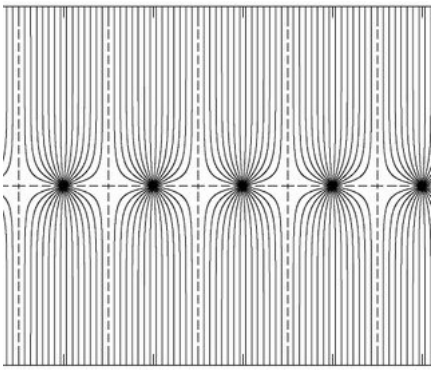

Figure 2.5: Cross-section of the multi-wire proportional chamber, where each black dot in the center is an anode wire and the top and bottom are the cathodes. The line are the field lines.

From figure 2.5 above, the benefit of having a MWPC chamber is clear, whereby each wire that picks a signal, can be isolated to an area within the field lines. The potential difference across MWPCs is usually set where a clear signal is obtained while maintaining the gain proportionality, this provides insight to the amount of charge lost in the ionisation event. An important aspect of the MWPC is the mechanical design, where Sauli[2] has calculated in traditional MWPCs that a diameter variation of 1% in the wires can result in a 3% change in gain and a 0.1 mm difference in the gap between the wires can result in about 15% gain difference.

2.2.3 Drift Chambers

The drift chamber is the umbrella term given to define the MWPC and drift region. This chamber has a moderate, uniform electric field that causes a drift of the electrons in the opposite direction of the field towards the anode wires, while the ions drift along the field to the cathode wires. The drift chamber enables determining the point of ionisation within the gas by measuring the transport time of the electrons from liberation to signal production and depending on which wire absorbed the electrons. Electrons produced at a time t_0 drift towards the anode wires at velocity w where an avalanche would occur at t_1, the distance of the initial electron would be given by:

$$x = \int_{t_0}^{t_1} w dt \quad [2] \tag{2.7}$$

which reduces to $x = (t_1 - t_0)w$ for a constant drift field [2]. The velocity of the electrons w is dependent on the potential difference across the planes. The positive ions created during the avalanche (as in figure 2.3) then propagate towards the cathode plane, inducing a positive signal.

Chapter 3

Experimental Setup

3.1 CERN

The Conseil Européen pour la Recherche Nucléaire, *CERN*, also known as the European Organisation for Nuclear Research, established 29 September 1954, is an international organisation that is located in the north western edge of Geneva, Switzerland, and borders with France, having 23 full member states [29].

The *Large Hadron Collider* (LHC), is the largest and most powerful particle accelerator in the world. It is the latest addition to the CERN accelerator structure, with a startup date of 10 September 2008. The LHC consists of a 27 km ring of superconducting magnets with accelerator structures designed to accelerate particles. The particles are injected into the LHC in opposite directions and accelerated to near the speed of light in a vacuum before they are steered to collisions by magnets. These collisions are controlled at the CERN Control Centre, and it is from the Control Centre that the particles are made to collide at 4 specific points along the LHC, corresponding to the 4 main detectors used, *ATLAS, CMS, LHCb* and *ALICE* [4].

ATLAS is one of the two general purpose detectors at the LHC designed for a wide range of functions, such as the search for the Higgs boson, extra-dimensions and particles that could make up dark matter. The *Compact Muon Solenoid*, CMS, is the other general purpose detector at the LHC, its physics programme ranges from studying the Standard Model of particle physics, along with extra dimensions and dark matter constituents. The *Large Hadron Collider beauty*, LHCb, is an experiment that was designed to investigate the differences between matter and anti-matter by focusing on a specific particle called the beauty quark, or b quark. ALICE, which houses the sub-detector of study (TRD), follows in section 3.2.

3.2 The ALICE Detector

A Large Ion Collider Experiment, or ALICE, weighing 10 000 tonnes with dimensions of 26m $\times$ 16m $\times$ 16m and based 56 m underground, is a detector designed and optimised to study heavy-ion collisions at ultra relativistic energies at the LHC and installed at interaction point 2 (IP2). The understanding is that collisions between heavy nuclei with a large centre of mass energy, at around 5.5 TeV per nucleon pair, would create a *Quark Gluon Plasma* (QGP). ALICE records the debris of these collisions and the ALICE

collaboration studies the resulting phenomenon, a process on a time scale of 0.1fm/c, with the aim of visualising and understanding the early time in our universe as well as answering fundamental questions about the matter in our universe today [29]. Figure 3.1 below shows the ALICE detector and its components.

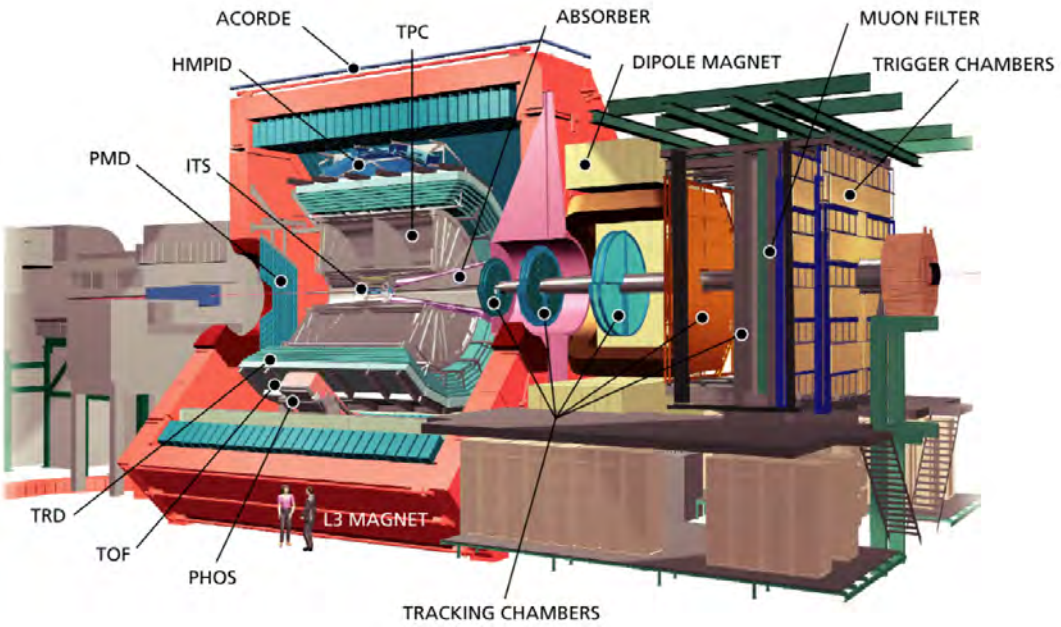

Figure 3.1: The ALICE detector and its components [4].

The central barrel of ALICE, with complete azimuthal coverage, consists of:

- *Time Projection Chamber* (TPC): Primary detector for charge and momentum determination of particles, using a specific energy loss methodology, the Bethe-Bloch curve, dE/dx, with full azimuthal angle coverage [12, 24].
- The *Inner Tracking System* (ITS): Serves to determine the primary vertex and secondary vertices for the reconstruction of charm, beauty and hyperon decays, it also serves as a particle identifier, tracking low energy particles and complimenting the TPC to improve momentum and trajectory measurements [13].
- A *Time of Flight* array (TOF): One of two detectors dedicated to *Particle Identification* (PID), the TOF chamber has an array of sub-detectors optimised for large acceptance of particle momenta with an upper limit of 2.5 GeV/c [14]. serves as a pre-shower detector [15].
- The *High Momentum Particle IDentification* detector (HMPID): The second detector dedicated to PID, it is a Ring Imaging Cherenkov (RICH) detector capable of detecting hadrons up to a momenta of 5 GeV/c. [22]
- The *Photon Spectrometer* (PHOS): A high granularity electromagnetic calorimeter with 17 280 detector channels of a Pb-W crystals and covers 100° in azimuthal angle.It is optimised for photon measurements in the energy range 0.5GeV/c − 10GeV/c, as well as π^o's of the range 1 GeV/c − 10 GeV/c and η mesons of the energy range 2 GeV/c − 10 GeV/c. It is capable of identifying higher energies, of course, this comes with a sacrifice of resolution [19].

- The *Transition Radiation Detector*: The detector of focus in this article, discussed in detail in the following section 3.3.

3.3 The Transition Radiation Detector

The ALICE *Transition Radiation Detector* (TRD) is found in between the TPC and TOF chambers within the ALICE detector, see figure 3.2. Its pseudo-rapidity η coverage, which is the angles covered from the beam axis with 0 being perpendicular to the beam, is $|\eta| \leq 0.84$, with the full azimuthal coverage (2π). Its total length spans 7 meters with a total detector area of 736 m^2. For its main task of efficient detection of electrons, the TRD consists of 18 supermodules, or sectors, each supermodule has 5 stacks (placed vertically) and 6 layers (placed horizontally) in the beam direction, as can be seen in figures 3.2 and 3.3, this gives the ALICE TRD a potential of housing $18 \times 6 \times 5 = 540$ individual readout chambers (ROCs). However, to allow access to the PHOS detector, the chambers on the center stack (one full layer) of supermodules 13, 14 and 15 are not installed, giving a total of 522 individual TRD read-out chambers. Each of these chambers contains specific components designed for specific tasks, these are the radiator (section 3.5.1), the multi-wire proportional readout chamber with drift region (section 3.6) and the front-end electronics (FEEs, section 3.5.2). Each chamber has a drift region of 3 cm with a gas mixture of Xe/CO_2 (85/15), where the CO_2 acts as a quenching gas, suppressing the propagation of photons which are produced when nuclei de-excite. The quenching gas acts to absorb these photons preventing them from ionising other molecules elsewhere in the gas chamber causing a loss of proportionality and accuracy, with the added safety feature of being non-flammable. The total gas volume of the TRD is 27 m^3. The drift region is separated from the amplification region of 0.7 cm by cathode wires, the drift time in the drift region is 2 µs with an electric field of 700 V/cm. In this specific gas mixture of Xe/CO_2 an ionising particle would liberate 275 e^-/cm with a gas gain of 5×10^3. The induced gas signal at the cathode plane is sampled in 30 time intervals spaced 100 ns over the drift region, each interval called a *time bin*, the collective sampling of the time bins is called an *event*. The nominal magnetic field on the TRD from the L3 magnet is 0.4 T, this causes a change in the drift direction of the beams, called the Lorentz angle, of 8° on the TRD [1]. A detailed summary of the ALICE TRD is given in table 3.1 below.

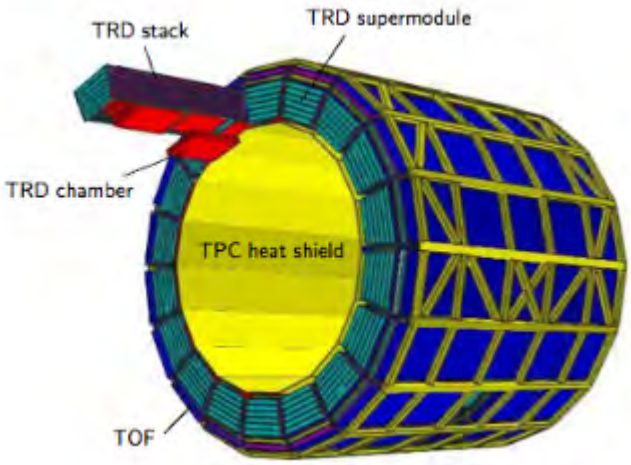

Figure 3.2: Configuration of the SMs at ALICE, the TRD stack shows the chambers and their orientation [4].

Each sector of the TRD can house $5 \times 6 = 30$ chambers, see figure 3.3, these are termed the super-modules (SMs), and ease the installation process by encompassing the 30 chambers to be fit as a single unit, there is a total of 18 super-modules [16].

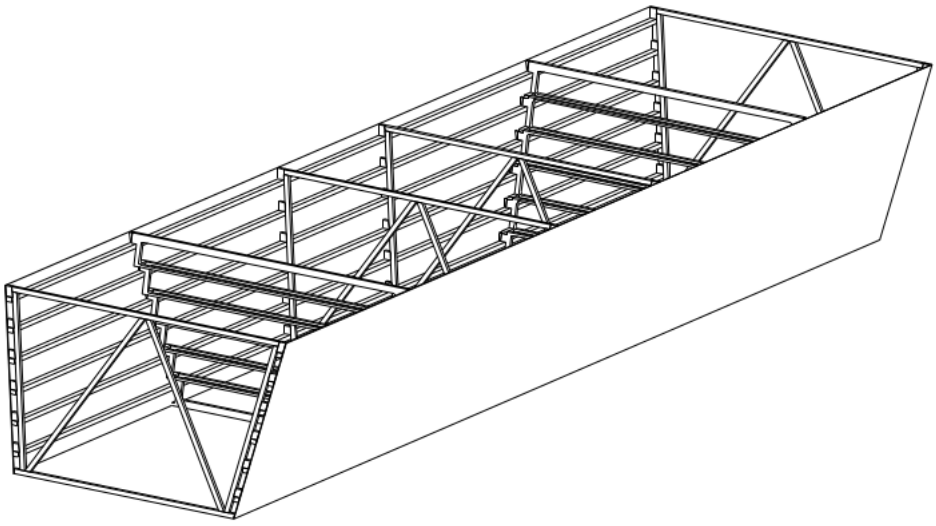

Figure 3.3: Skeleton view of one of the 18 TRD super-modules, with 6 rows and 5 columns for the 30 chambers [1].

Parameters	**Values**
Pseudo-rapidity coverage	$-0.84 < \eta < +0.84$
Azimuthal coverage φ	60°
Radial position	2.90 m to 3.68 m
Length of a super-module	7.02 m
Weight of a super-module	1.65 tonnes
Segmentation in φ	18 sectors
Segmentation in z_{lab}	5 stacks
Segmentation in r	6 layers
Total number of read-out chambers	521
Size of a read-out chamber (active area)	0.90 m x 1.06 m to 1.13 m x 1.43 m
Radiator material	fibre/foam sandwich
Depth of radiator	4.7 cm
Depth of drift region	3.0 cm
Depth of amplification region	0.7 cm
Number of time bins (100 ns)	30
Total number of read-out pads	1 150 848
Total active area	673.4m^2
Detector gas	Xe-$CO_2(85-15)$
Gas volume	27m^3
Drift voltage (nominal)	$\sim$ 2150V
Anode voltage (nominal)	$\sim$ 1520V
Gas gain (nominal)	$\sim$ 3200
Drift field	$\sim$ 700V/cm
Drift velocity	$\sim$ 1.56cm/micros
Avg. radiation length along r(X/X_0)	24.7%

Table 3.1: Summary of the ALICE TRD parameters and specifications.

3.4 The ALICE Transition Radiation Detector Chamber

Transition Radiation (TR) occurs when a particle crosses a boundary in between two different media with different dielectric constants. The energy of the photons produced extends into the X-ray energy range for relativistic particles ($\gamma \geq 1000$). The transition photon released is in the same direction as the particle traversing the chamber. Each chamber in the TRD has a drift region to allow for the reconstruction of the particles, working in conjunction with the TPC and ITS at high multiplicities.

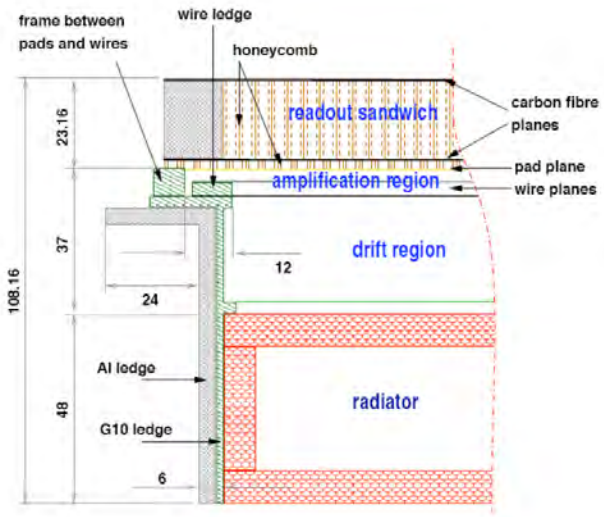

Figure 3.4: Cross-sectional of the TRD Readout Chamber [4].

Figure 3.4 above gives the cross-sectional view of the chamber. If and when a charged particle enters into the drift region, it produces electrons by ionising the gas within the drift region. Due to the potential difference across in the drift region, the liberated electrons drift towards the anode wires and create an avalanche effect when in close proximity. The positive ions created during this avalanche drift in the opposite direction, towards the pad plane [4].

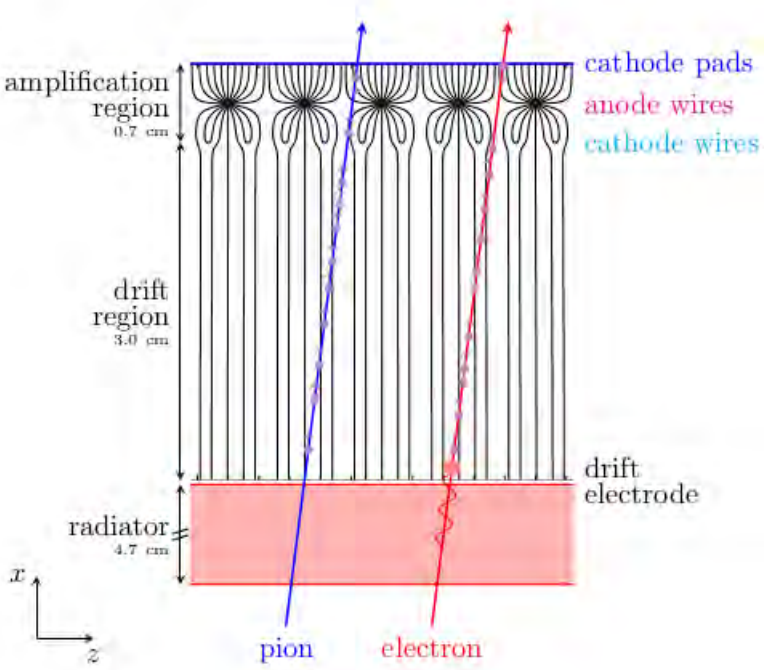

Figure 3.5: Cross-sectional view of the three regions of the chamber, the radiator, the drift region and the amplification region. A pion and an electron traversing illustrate the ionisation energy deposition and transition radiation contribution. The energy deposition due to the TR photon absorption is shown by the red dot in the drift region. The figure is not drawn to scale. [16].

It is important to note that, within the ALICE TRD, the chambers do differ in design size. A summary of the ALICE TRD chambers is given in table 3.2 below.

Name	L_z	$W_{r\phi}$	No. of rows	α_{tilt}	L_{opads}	L_{ipads}	W_{opads}	W_{opads}
L0C0	1080	922	12	-2	80	90	5.15	6.35
L0C1	1220	922	16	-2	75	75	5.15	6.35
L1C0	1080	966	12	+2	80	90	5.85	6.65
L1C1	1220	966	16	+2	75	75	5.15	6.65
L2C0	1080	1011	12	-2	80	90	7.05	6.95
L2C1	1290	1011	16	-2	75	80	7.05	6.95
L3C0	1080	1055	12	+2	80	90	7.75	7.25
L3C1	1360	1055	16	+2	75	85	7.75	7.25
L4C0	1080	1099	12	-2	80	90	8.45	7.55
L4C1	1430	1099	16	-2	75	90	8.45	7.55
L5C0	1080	1144	12	+2	80	90	9.65	7.85
L5C1	1450	1144	16	+2	85	90	9.65	7.85

Table 3.2: Name, size and dimensions of the different design chambers installed within the ALICE TRD [4].

From table 3.2 above, L_z gives the length, $W_{r\phi}$ the width, α_{tilt} gives the angle by which the pads are tilted with respect to the z-axis, the subscripts *opad* and *ipad* gives the lengths across the outer and inner pads respectively, units are in millimetres. For this project, an L3C0 chamber was used, containing 12 pad rows, each with 144 pads (discussed in detail in section 3.7).

3.5 Mechanical Design

3.5.1 Radiator

As stated earlier in section 3.4, transition radiation is produced when a relativistic charged particle traverses a boundary between two media with different dielectric constants, but the likelihood of producing a transition radiation photon is small, thus leading to a need for a large number of transition media to increase the chances of a transition radiation photon to be produced [1].

This is done with the radiator, where polypropylene fibre sheets5 mm thick are stacked with a regular periodic structure and sandwiched between 8 mm plates of Rohacell foam HF71, which are then reinforced by fibre sheets, figure 3.6 below describes this sandwich [4]. These stacks provide multiple interfaces with different dielectric constants, each having the possibility of producing transition radiation as a charged particles traverses. The radiator also supports the front window of the chamber, as well serves as the drift electrode.

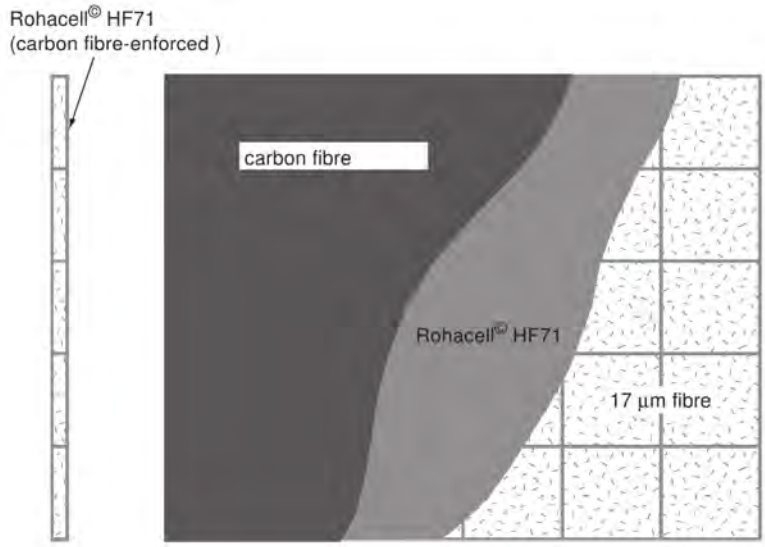

Figure 3.6: Side view (left) and top view cross-section (right) of the radiator design, where the stacked carbon fibre is covered by the HF71 foam, which in turn is reinforced by fibre sheets. [1].

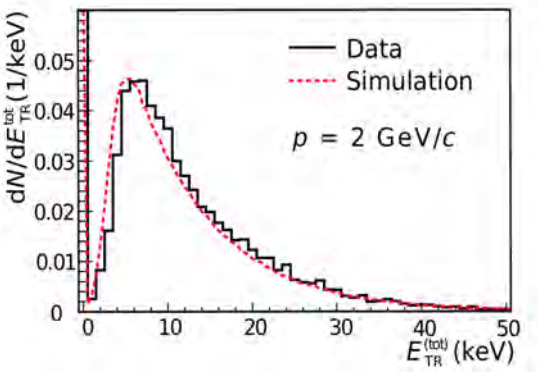

(a) Simulated and measured TR momentum production for 2GeV/c electrons for the sandwiched design [16].

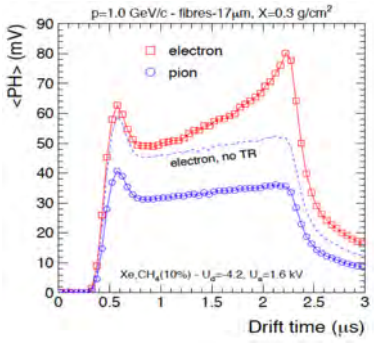

(b) The average pulse-height vs drift time of the sandwiched radiator at 1GeV/c, visualising TR contribution to the detected electron signal [4].

Figure 3.7: Statistical data results for the sandwich design of the radiator [1].

While different designs of a radiator have been created and tested, there are limitations that need to be considered when designing the radiator. Space requirement within the TRD is one, the others would be cost, efficiency and mechanical stability [20]. An in depth analysis of the comparisons between the different radiator designs can be found on [21].

3.5.2 Front End Electronics

As the particle traverses the radiator, it both creates transition radiation and deposits energy in the drift chamber, the path followed by the particle in the chamber, is called a tracklet. The path followed by the particle across the entire TRD stack (as described in section 3.3) is called a track. Once a signal is induced on the wires within the chamber, the *Front End Electronics* (FEEs) are used to read these signals. The ALICE TRD consists of 1.156×10^6 channels and consists of multiple components that work to restructure the

induced signal for presentation, see figure 3.8 below for a graphical representation and short description of their specific tasks.

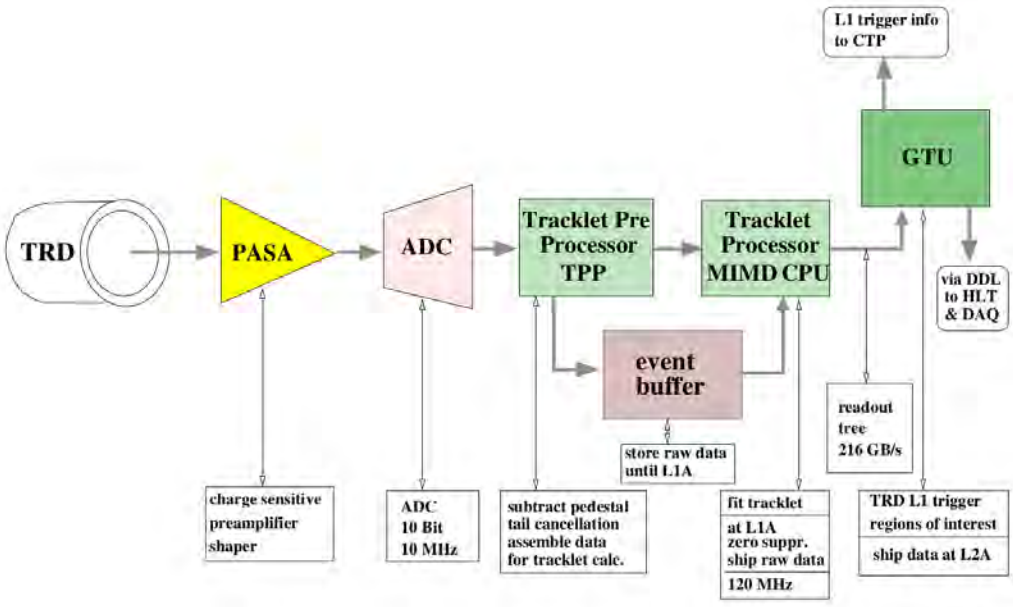

Figure 3.8: Electronic makeup of the FEEs [1].

The charge sensitive *PreAmplifierShAper*, PASA, is used for noise reduction from the signal. The *Analog to Digital Converter*, ADC, is a low power analog chip that is connected to the digital circuitry, in which data is processed and stored in event buffers for readout. The *Tracklet Pre-Processor*, TPP, is used to prepare the data for the *Tracklet processor*, TP, during the drift period. At the end of the drift time, the TP, which is a micro computer chip operating at 120MHz denoted as a *Multiple Instruction Multiple Data* (MIMD) processor, processes all the data to identify potential tracklets. The potential tracklet data is then shipped to the *Global Tracking Unit*, GTU, which combines the information from the individual tracklet chambers [25], to create a track for the particle.

The limitations of power consumption and cost has instigated the production of multiple channels into a single unit referred to as the *Multi-Chip Module*, or MCM. The MCM, the ADCs, the tracklet processor and MIMD, as a set, are referred to as the *Local Tracklet Unit* (LTU) [25]. There are 64 224 MCMs mounted on the ALICE TRD, and all signals that connect the MCMs are routed through the motherboard. There are 8 MCMs per pad row on the chamber, this is due to limitations of size and cost.

3.6 The TRD Multi-Wire Proportional Chamber

The average number of electrons produced by an ionising particle, 275 e^-/cm, is not sufficient to produce a measurable signal, thus requires further amplification. This process of amplification of the signal is done with the use of wires on two different planes running in the azimuthal angle. The MWPC houses these wires in the amplification region of the TRD chamber, with a thickness of 7 mm. This region has the anode wires placed at the center 3.5 mm from both the cathode wire plane and the pad plane. Thus, the anode wires lie directly in between the cathode wire plane and the pad plane [4], see figure 3.9 below.

The MWPC provides the environment required to produce gas amplification, giving rise to an avalanche effect.

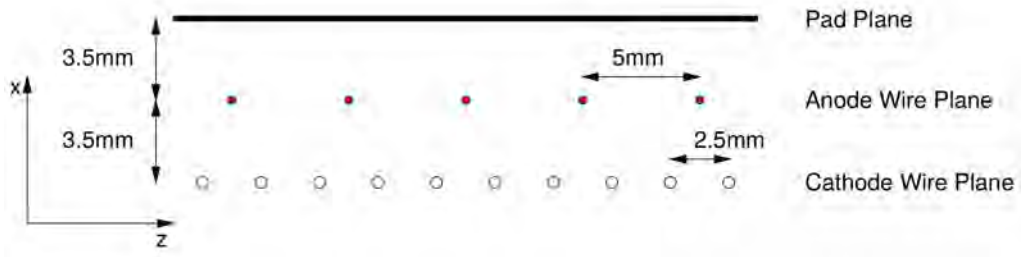

Figure 3.9: Graphical representation of the wire geometry within the MWPC [1].

The amplification region, with relation to the TRD chamber (figure 3.4), sits on top of the drift region and is separated by the cathode wires, which act as a divisor of the drift region and the amplification region and has a ground potential. Thus, electrons produced within the drift region are only accelerated towards the anode wires once they have passed the cathode wires and start an avalanche close to the anode wires, where a positive potential is applied [1]. Table 3.3 outlines the specifics of the chamber wires.

As mentioned in section 2.2.1, an RC circuit can be integrated into the system in order to obtain low impedance terminations with an increase in the rate capability of the counter. This is done using a two stage filter within the chamber, which is installed in the HV filter box mounted on the side of the chamber. The HV filter box supplies the anode and cathode wires with the HV. The 4.7 nF and 2.2 nF capacitors then suppress the load induced fluctuations of the voltages in the chamber [16], since the capacitors cannot charge, or discharge, instantaneously. Figure 3.10 shows the two stage low pass filter in the TRD MWPC. The first stage low pass filter has already been removed at CERN (4.7 nF capacitors).

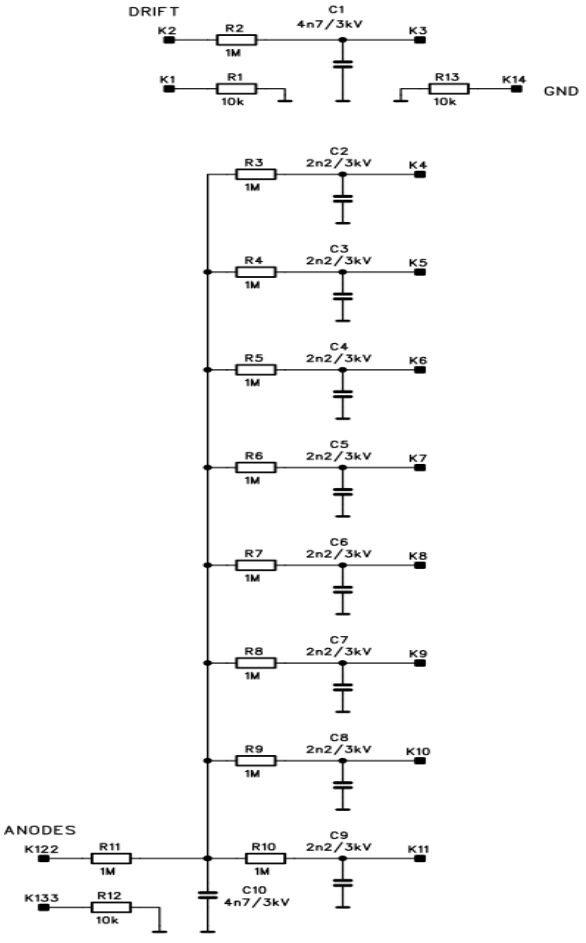

Figure 3.10: Circuit diagram of capacitors, along with the resistors [5].

	Anode Wires	**Cathode Wires**
Material	Au plated W	Cu/Be
Diameter	20 µm	75 µm
Tension	0.45 N	1.2 N
Length	$100 - 120$ cm	$100 - 120$ cm
Pitch	5 mm	2.5 mm
Total number in TRD	140 000	280 000

Table 3.3: MWPC specifications [1].

To calculate the inherent capacitance of the chamber itself, consider an anode wire, along with the pad plane on top, the adjacent anode wires, and the cathode plane underneath. Starting with the electric field equation along a wire:

$$E(r) = \frac{\lambda}{2\pi\epsilon_0 r} \tag{3.1}$$

where λ is the charge per unit length on the wire, ϵ_0 is the permittivity of vacuum and r is the distance from the centre of the wire to a point of interest. The electric potential V at a distance r from the anode wire of radius a would be:

$$V(r) = V(wire) + \int_a^r -E(r)\mathrm{d}r = V(wire) - \frac{\lambda}{2\pi\epsilon_0}\ \ln\left(\frac{r}{a}\right) \tag{3.2}$$

The pad plane within the TRD is grounded, thus has a potential of 0, for a wire with radius a, of length L that is a distance h from the pad plane, with an arbitrary radius of interest within the wire s, the potential for a *positive* and *negative* charge electrode wire can be given by:

$$V = V_{(+s)} - \frac{\lambda}{2\pi\epsilon_0}\ \ln\left(\frac{\sqrt{(x-s)^2+y^2}}{a}\right) + V_{(-s)} - \frac{-\lambda}{2\pi\epsilon_0}\ \ln\left(\frac{\sqrt{(x+s)^2+y^2}}{a}\right) \tag{3.3}$$

With the above giving:

$$V = \frac{\lambda}{2\pi\epsilon_0}\ \ln\sqrt{\frac{(x+s)^2+y^2}{(x-s)^2+y^2}}$$

Since $V_{+s} + V_{-s} = 0$, the term under the square root sign signifies the equipotential circle, dubbing this as O:

$$O = \sqrt{\frac{(x+s)^2+y^2}{(x-s)^2+y^2}}$$

$$\left(x - s\frac{O^2+1}{O^2-1}\right)^2 + y^2 = \left(s\frac{2O}{O^2-1}\right)^2$$

where s and O fit the equipotential borders of the wire:

$$s\frac{O^2+1}{O^2-1} = \pm h, \quad s\frac{2O}{O^2-1} = a$$

where h is the distance between the centre of the wire and the pad plane. Therefore:

$$O = \frac{h}{a} \pm \sqrt{\left(\frac{h}{a}\right)^2 - 1}, \quad s = \pm\sqrt{h^2 - a^2}$$

Thus, for a given wire of line charge λ, radius a, and distance h from the pad plane, the potential would be:

$$V = \frac{\lambda}{2\pi\epsilon_0} \ln\left(\frac{h}{a} + \sqrt{\left(\frac{h}{a}\right)^2 - 1}\right) \tag{3.4}$$

To then determine the capacitance, with $\lambda = \frac{Q}{L}$:

$$C = \frac{Q}{V} = \frac{Q}{\frac{Q}{2\pi\epsilon_0 L} \ln\left(\frac{h}{a} + \sqrt{\left(\frac{h}{a}\right)^2 - 1}\right)} \tag{3.5}$$

$$C = \frac{2\pi\epsilon_0 L}{\ln\left(\frac{h}{a} + \sqrt{\left(\frac{h}{a}\right)^2 - 1}\right)} \tag{3.6}$$

Equation 3.6 above gives the capacitance between a wire and an even grounded plane, in this case, the pad plane above the anode wires and the cathode wires below. Note that the cathode wires are not a plane, but are assumed to be.

For the capacitance between the anode wires themselves, starting with the electric field of a charged wire:

$$E(r) = \frac{\lambda}{2\pi\epsilon_0 r}$$

The potential difference across the wire, relative to the adjacent wire a distance d away, would be given as:

$$V = \int_a^d -E(r)\mathrm{d}r = \frac{\lambda}{2\pi\epsilon_0} \ln\left(\frac{d}{a}\right)$$

For two wires, of similar charge and length L:

$$V = \frac{1}{2\pi\epsilon_0}\left(\lambda \ln\left(\frac{d}{a}\right) + \lambda \ln\left(\frac{d}{a}\right)\right)$$

$$V = \frac{\lambda}{\pi\epsilon_0} \ln\left(\frac{d}{a}\right)$$

Thus, the capacitance between the two wires, with $\lambda = \frac{Q}{L}$ would be:

$$C = \frac{Q}{V} = \frac{Q}{\frac{Q}{\pi\epsilon_0 L} \ln\left(\frac{d}{a}\right)} = \frac{\pi\epsilon_0 L}{\ln\left(\frac{d}{a}\right)} \tag{3.7}$$

The above are specific to the chamber studied and thus would give a capacitance specific to the mechanical design of the chamber. In this case, the ALICE TRD chamber.

3.7 University of Cape Town Read Out Chamber

3.7.1 Design

The *University of Cape Town*, UCT, houses a TRD Read Out Chamber (ROC) in the department of physics. The ROC is a L3C0 chamber (see table 3.2 for specifications)

with the pad plane segmented into 12 pad rows and 144 pad columns, the thickness of the pad rows allows for 17 anode wires, spanning across all 144 pad columns. The chambers detector electronics are also separated into 6 read out boards (ROB), each having their own low voltage power supply.

The computer in the TRD room runs a Linux operating system used as an interface to communicate with the TRD chamber using a *Distributed Information Management* (DIM) system, which is a communication system between mixed environments used primarily at CERN. The computer also has installed the *Data Acquisition Software*, or DAQ, which allows for communication between the computer and the logic box(discussed further in section 3.7.2) [25]. The setup of the room is shown below on figure 3.11.

Figure 3.11: Image of the UCT TRD chamber, to the left is the gas supply (Ar-CO_2), behind the chamber is the low voltage supply for the ROBs, below the chamber is the scintillation detector used as a trigger and to the right of the chamber is the TRD box.

The high voltage (HV) supply to the chamber is provided by the NHQ HV power supply unit (PSU) [28] attached to the VIM crate (see section 3.7.2), this supplies the anode wires and the voltage across the drift region.

The high voltage supply, is delivered to the chamber via the high voltage filter box, here six (6) 2.2 nF capacitors and two (2) 4.7 nF capacitors are installed. Each high voltage supply line from the filter box provides for 2 pad rows (forming a HV segment). Thus, there is a total of 6 high voltage segment supply lines within the filter box. Each HV segment caters for a pad row and its pad row sibling (forming a pad row pair), since the chamber has 12 pad rows (L3C0), it has 6 pad row pairs, thus six (6) 2.2 nF capacitors.

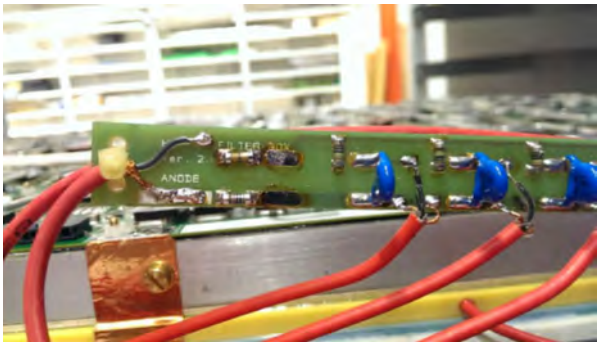

(a) Image of the 2.2 nF capacitors installed within the chamber.

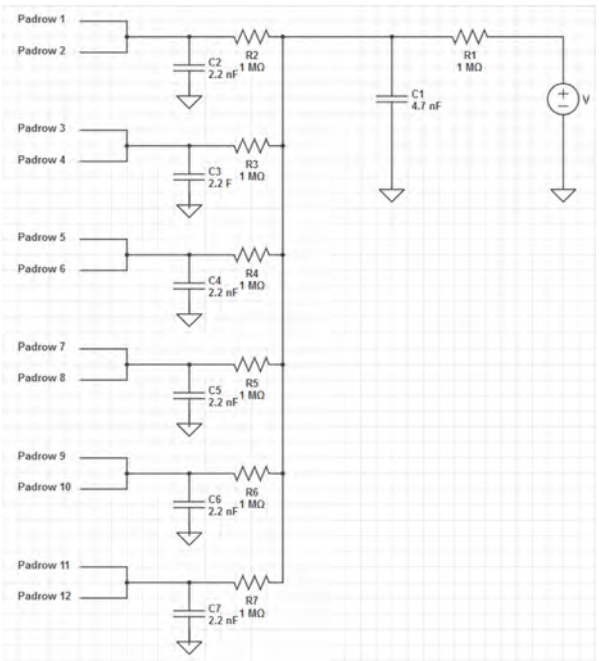

(b) Circuit diagram of the UCT L3C0 anode voltage supply, C1 has already been removed.

Figure 3.12: Capacitors of the TRD chamber.

These capacitors are prone to failure, this causes a dead chamber, which cannot be used to acquire data for the remainder of run, hence its removal. Figure 3.12b shows the circuit of the low pass filter design used in the chamber, note that the first stage low pass filter, the C1 capacitor, has been removed and this experiment tests the system after removal of capacitors C2 to C7.

The TRD chamber at UCT is used to acquire data, then have its 2.2 nF capacitors removed, as shown in figure 3.13 below, this allowed for the full testing of the system with and without the capacitors.

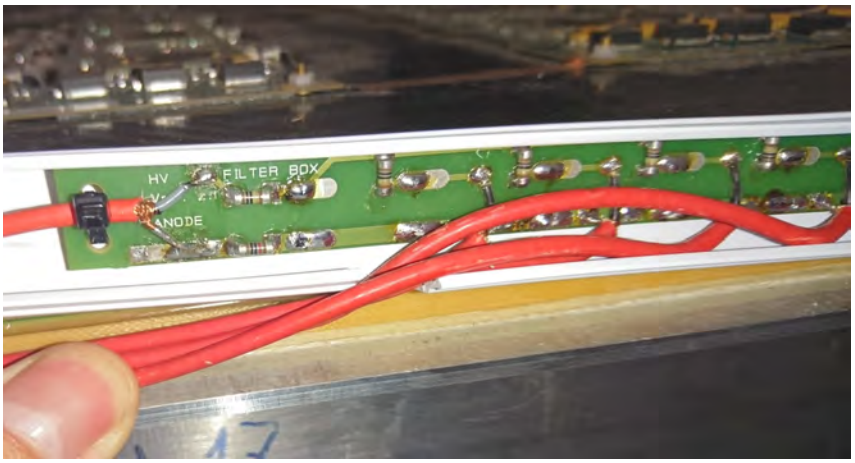

Figure 3.13: The UCT chamber filter box with removed capacitors.

As mentioned in section 3.3, the gas used at CERN is a Xe/CO_2 mix with a (85/15) ratio. However, due to the cost of this gas, it is not economical to reproduce this at UCT. The alternative is Ar/CO_2 (85/15), which has an electron range (distance electron

can traverse before stopping) of approximately a factor of 5 smaller, but has a similar relationship as a function of electron energy, see figure 3.14.

The gas used at the UCT chamber is a mixture of Ar/CO_2 (75/25), as opposed to the Ar/CO_2 (85/15) shown in figure 3.14, which, at the time of the experiment, was not readily available and must have been custom made (or imported), as opposed to the industrial grade Ar/CO_2 (75/25). Considering the projects use of Ar/CO_2 (75/25) and the CO_2 use as a quenching gas, a higher Ar concentration would lead to a larger gain. There should be no difference on the study of the baseline, considering the primary concern being the amount of charge absorption on the wires. Due to the nature of the gas and the need for consistency, the chamber is first flushed for 12 hours at a high flow rate with the Ar/CO_2 gas mixture, after which the flow rate is decreased and stabilised for a few more hours before data is then collected.

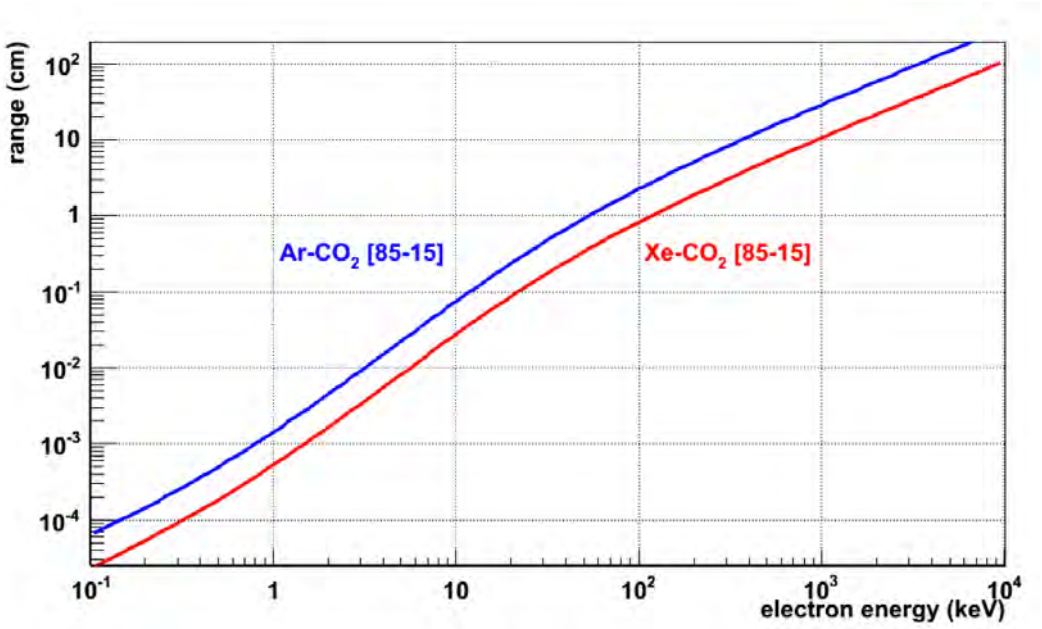

Figure 3.14: Range of electrons as a function of energy for two gas mixtures, Xe-CO_2 and Ar-CO_2, both at a ratio of 85-15. The graph is logarithmic, showing a difference in range of approximately a factor of 5. The shorter range of Xe-CO_2 can be attributed to its higher density [4].

3.7.2 TRD Box

The TRDbox is a module used for data acquisition (DAQ) based on Field Programmable Gate Arrays (FPGA), an integrated circuit device configurable via programmable interfaces. It's located within the VIM crate (figure 3.15 below), which also houses the HV power supply. The TRDbox consists of an SU704 FPGA and SU738 FPGA logic boxes, which handles the triggers from the scintillation detector (section 3.7.3) and the aforementioned DAQ software, it is controlled by a Linux program called *trdbox*. A thorough look at the TRDbox and its component logic boxes is outside the scope of this dissertation [7].

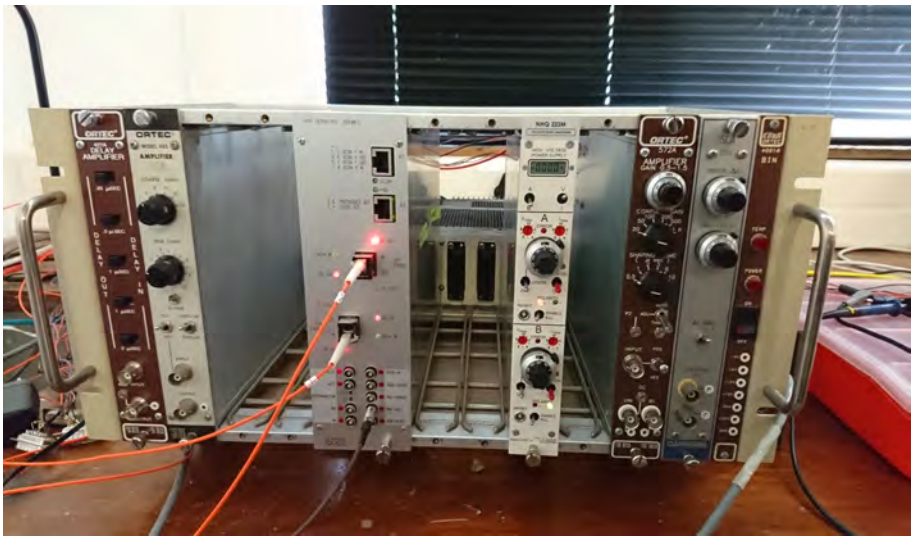

Figure 3.15: UCT VIM crate, with the logic boxes and HV power supply shown (only modules used).

3.7.3 Triggering Mechanism(Scintillation Detector)

The triggering mechanism used is a scintillation detector, placed underneath the chamber and is connected to the VIM crate with a total surface area of 0.5 m^2. It consists of a scintillation plate, a light guide and a Photo-Multiplier Tube (PMT), depicted in figure 3.16 below.

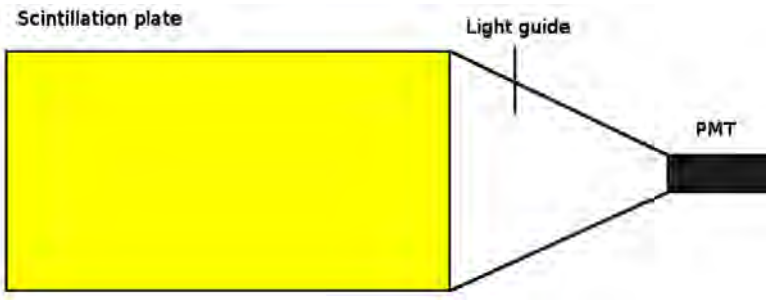

Figure 3.16: Schematic of the scintillation detector used as a trigger [26].

After the particle traverses the TRD chamber, it propagates to the scintillation detector below, where it interacts. The scintillator acts to produce light when a charged particle interacts within it, with a proportionality between the amount of energy deposited and the amount of light produced. The light guide, as the name suggests, serves to guide the light photons produced to the PMT, where the light photons liberate electrons, which are then multiplied by the dynodes within the PMT to amplify the signal and create a current [26]. If the signal is above a user specified threshold, this signal acts as the trigger, instructing the TRDbox to instruct the FEEs of the chamber to collect data, which is then stored in the computer.

Chapter 4

Analysis & Results

4.1 Data Sets and Parameters

For the experiment, multiple runs (data acquisition from the chamber at UCT) were taken into consideration. However, run 0499 with the capacitors installed and run 0518 with the capacitors removed were selected due to their similarities in charge absorption and number of events, which are sampled 30 times over 100 ns 3.3. An added run, run 0517 - without capacitors, is also included in the analysis and results, with the same setup as run 0518, but with an anode voltage AV = 1500V. This would be to both test if truly, the baseline shift is independent of the anode voltage, as well as verify that the effects of a high tracklet count within CERN can be replicated within UCT by having a high gain.

Both of these runs were non-zero (NZ) suppressed runs, thus any signal produced at the detector is recorded, resulting in the acquisition of all data, irrespective of a tracklet going through or not, as opposed to zero (Z) suppressed runs, which would only record signals above a specific threshold. The data acquired at CERN is zero suppressed data, considering the phenomenon of study (the baseline shift), it could not be used in this analysis project because no additional information is given on any other detector pads other than those with a particle traversing. Furthermore, due to NZ suppressed runs acquiring all data within the chamber, the files are on average 34 times larger than a Z suppressed run (at UCT) for a similar number of events. Considering the massive runs at CERN, data storage is a factor to strongly account for, hence the use of Z suppressed data.

For each run in this analysis, a total of 10,000 events were recorded, where the anode and drift voltages were set to 1600V and 2000V respectively, with the gas flow maintained at 6 m^3/hr after a 12 hour flush of the gas chamber at 16 m^3/hr.

Run 0499 has a total of 5349 events with a tracklet, however only 3723 events were considered during this study. Run 0518 has a total of 5524 events with tracklets and 3755 events were considered. A large amount of the events not considered is due to tracklets falling below the user set lower limit of energy, 2,500 ADC counts, this is to ensure only higher energy particles are considered for discernible results of the common-mode effect. A small amount is due to tracklets having higher than the set upper limit of energy, 17,500 ADC counts, this is because particles above this range are very few and thus do not provide the sample size required for a reliable statistical analysis. The remainder is due to the more than a single tracklet going traversing the chamber at a given event (see

section 4.1.1). Table 4.1 below gives the total breakdown of events.

Description	0499	0518
No tracklets	4 656	4 477
$>$ 1 tracklet	1 620	1 767
1 tracklet	3 723	3 755
Total events	9 999	9 999

Table 4.1: Table of the tracklet numbers of the runs. The total number falls to 9 999 due to the first event being a configuration event.

With the 10,000 events for each data set, the events are separated into two different groups, one where there were no tracklets that traversed the chamber and one where there was a tracklet that traversed (event of interest). The energy absorbed within the chamber in the events of interest (EOI) reflects as ADC counts, which is separated into bins of 750 ADC values from 2,500 ADC counts to 10,000 ADC counts, from 10,000 ADC counts to 17,500 ADC counts the bin size is increased to 2,500 ADC counts, leading to a total of 13 energy bins (see section 4.1.1). This binning process and size is needed for both determination of the shift in baseline with relation to the amount of charge absorbed, as well as give accurate statistics by having a reliable sample size within the energy bin.

The EOI tracklet path, energy absorbed as well as the number of pads involved is recorded and visualised. The data on the pads associated with the tracklet, plus 2 pads on both sides, is then extracted to determine the EOI's corresponding energy bin. The pads involved in the interaction are then masked out to have no contribution when determining the average baseline of the remaining pads, which give the baseline shift as a function of time for the energy bins. Once the pad row of interaction is isolated, its corresponding pad row sibling is analysed as well (those without a tracklet), this data of the event is then compared to the remaining pad rows without a tracklet within the same event.

The baseline of the runs is then analysed and compared to understand the effect of having the capacitors removed, these effects are then corrected for.

With the behaviour and parameters at hand, the regions of interest (ROI) are defined to identify the tracklets within the events, as shown in figure 4.2.

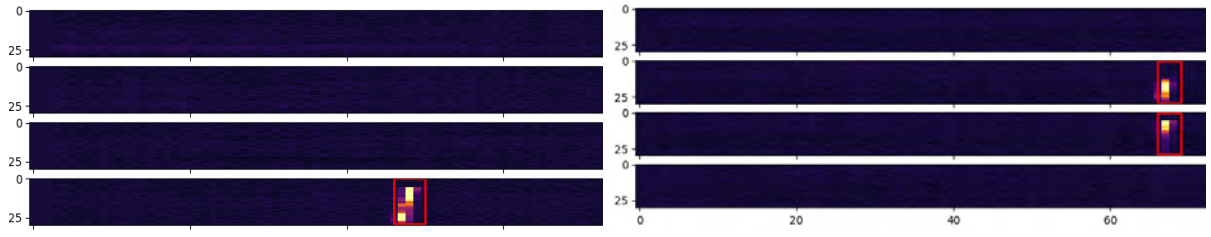

(a) ROI of a single tracklet, ROB4.

(b) ROI two tracklets, ROB0.

Figure 4.2: Defining the regions of interest, each horizontal bar is a pad row, the red borders show the tracklet in the event, it is from these borders that 2 pads are counted on both directions along the same pad row to isolate the region.

Due to the phenomenon in question and the uncertain effects it has on the surrounding pads and pad rows, only events with a single tracklet are considered for analysis.

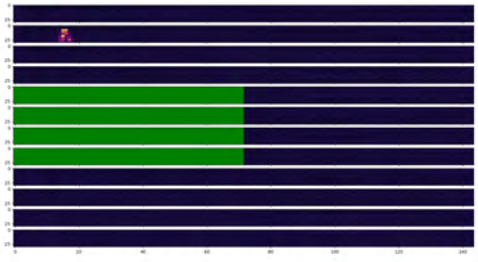

(a) Single tracklet, event considered.

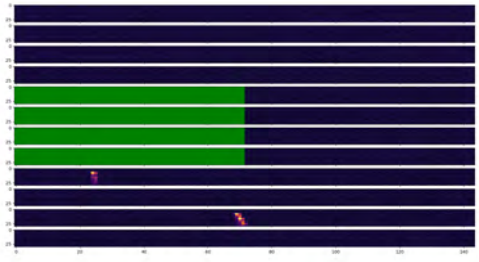

(b) 2 tracklets, event not considered.

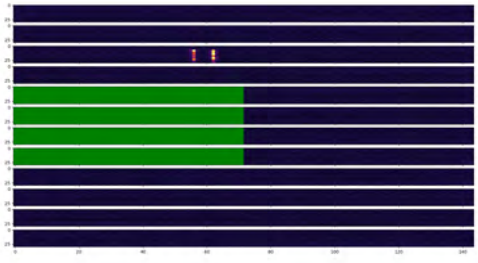

(c) 2 tracklets on a single pad row, event not considered.

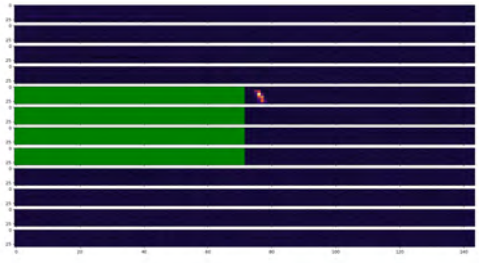

(d) single tracklet on pad row 4, event not considered due to being on a the masked pad row.

Figure 4.4: Event display showing tracklets in the chamber, where each horizontal bar is a pad row, consisting of 144 pads stretched horizontally with time set vertically. The green bars depict a ROB masked due to a LV supply issue, described further in section 4.1.1.

4.1.1 Limitations

ROB 2 (Readout board 2) of the chamber, which covers pad row 4 to 7 and pads 0 to 72 has a low voltage supply issue, this leads it to give high readings across the entire board. For this reason, a mask is applied on this ROB during the analysis phase to neglect all its values and all tracklets are thus omitted. See figure 4.6 below. For consistency, since the common mode effect is experienced at surrounding detector pads within the same pad row, the effect of not having any data from ROB 2 on ROB 3 with the same HV supply is not known. For this reason all particles traversing ROB 2 and ROB 3 are omitted from the analysis.

(a) Event display with ROB2.

(b) Event display with ROB2 masked.

Figure 4.6: Depiction of the issue with ROB2, each horizontal line row represents a pad row, the pads are along the $x-$direction, with time bins represented on the $y-$direction of each pad row. Without and with the mask applied, images are of the same event with a tracklet.

A high incidence rate in a certain energy bin is required to provide adequate statistical data within that energy region for a reliable analysis, above 17,500 ADC counts, as energy increases, the number of charge absorption incidences in that energy bin decreases, leading to a smaller sample size and thus would sacrifice accuracy and precision should they be included. Hence, they are omitted.

4.2 Analysis

4.2.1 With Capacitors - Run 0499

As stated, the NZ suppressed run is carried out with capacitors for 10,000 events, the energy distribution histogram is shown in figure 4.7 below, to show the number of incidences for a specific amount of charge absorbed:

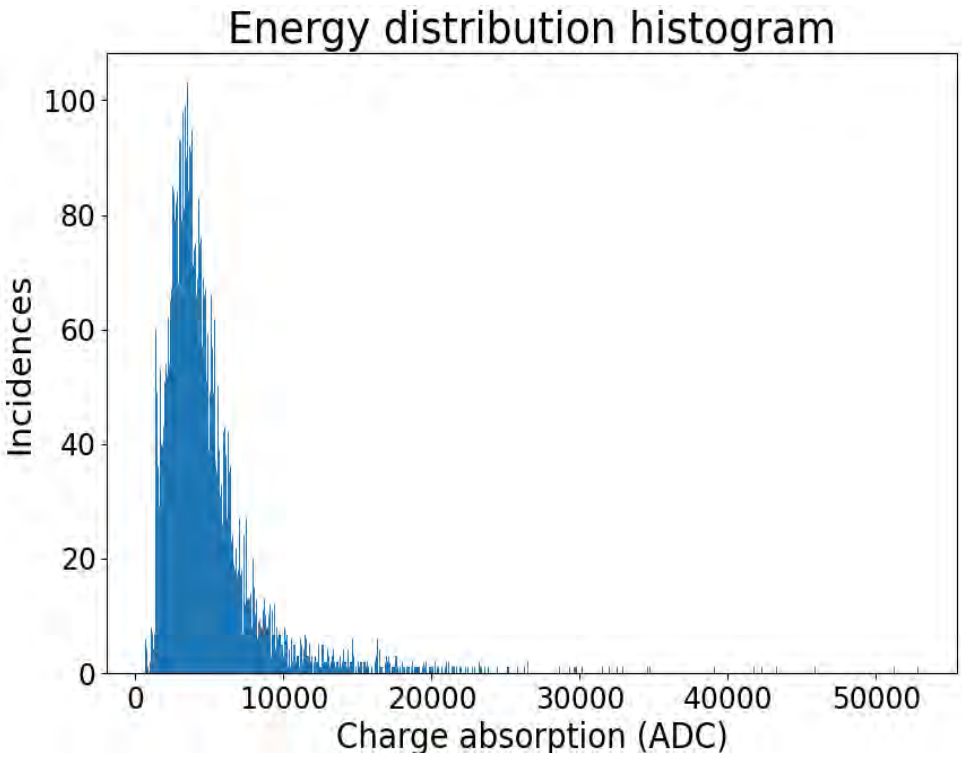

Figure 4.7: Energy distribution histogram for run 0499. The peak with the highest number of incidence, 103, centres on 3526 ADC.

Figure 4.7 represents the energy distribution of run 0499 with capacitors, a bin size of 52 is used, hence all ADC values falling within a specific, discrete range in steps of 52, are grouped into a single bin. A total of 1000 bins were used. Thus, for the point of highest incidence (103 counts), the energy range is 3526 ± 26 ADC values.

Run 0499 has an anode voltage of 1600V and drift voltage of 2000V. Figure 4.8 below shows the average signal produced in ADC for the events considered in the run, also called the pulse height plot.

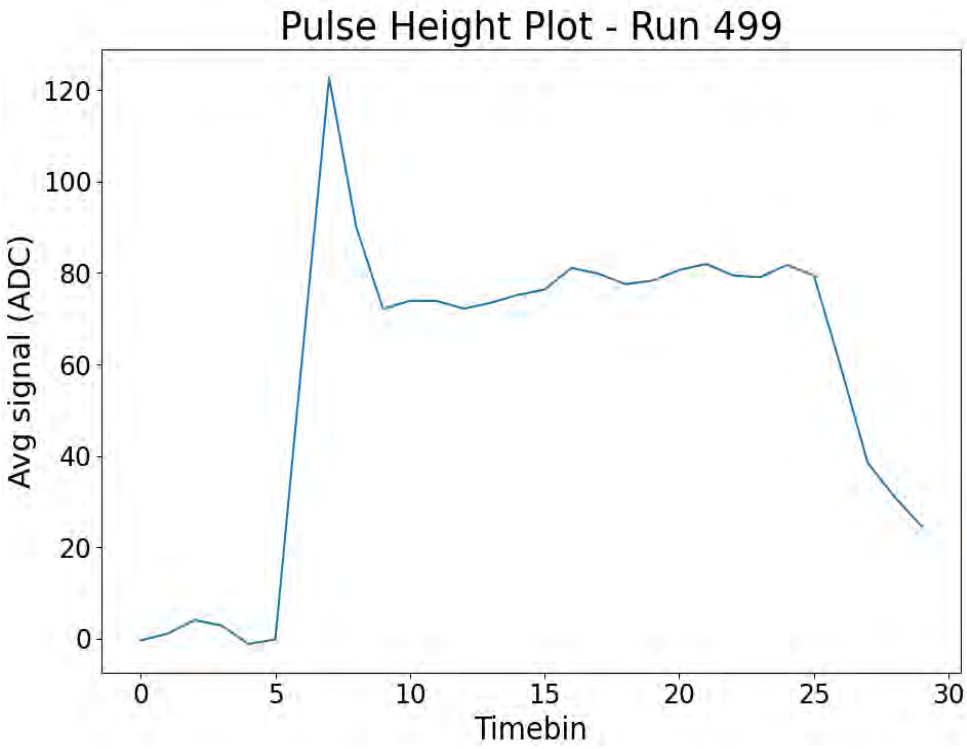

Figure 4.8: The pulse height plot of run 0499 showing the average signal pulse as a function of time, which plateaus at around 80 ADC.

The initial phase of figure 4.8, up to time bin 5, shows the delay before the signal is received by the FEEs to collect data, where there is a large sum of electrons by this time, hence the spike. Once the electrons are collected from the immediate vicinity of the anode wire, the average energy uptake drops back to a nominal value that is dependent on the parameters set. The plateau shows the average signal produced and thus this gives a representation of the average number of electrons absorbed, the average energy of this plateau is mostly affected by the anode voltage, where a higher anode voltage causes a larger average energy of the plateau. The drop off at end of the curve is the near final absorption of the electrons liberated by the tracklet, and is mostly affected by the drift voltage set.

Table 4.2 shows the tracklet energy distribution within the run. For bin 14, where the charge absorption range was $>$ 17500 ADC, though the incidence number is higher than the previous bin (18 for bin 14 compared to 16 of bin 13), it is omitted since it would not have offered any reliable data or statistics due to the vast range in charge absorption(refer to figure 4.7) .

With the binning procedure (table 4.2), the data is dissected once more into three groups, the pad rows of tracklet interaction, its adjacent pad row sibling which has the same high voltage supply, the average of the remaining pad rows in the event that did not have a tracklet going through. These three groups are then plotted, along with the average baseline of events with no tracklets, to analyse the results. Figures 4.9 and 4.10 below show the baseline as a function of time for energy bins 4 and 11 respectively:

Bin	Energy range (ADC)	Incidences	Avg Charge Absorption q (ADC)
0	< 2500	353	1982
1	$2500 - 3250$	602	2917
2	$3250 - 4000$	716	3632
3	$4000 - 4750$	633	4374
4	$4750 - 5500$	456	5103
5	$5500 - 6250$	335	5854
6	$6250 - 7000$	195	6577
7	$7000 - 7750$	127	7367
8	$7750 - 8500$	85	8063
9	$8500 - 9250$	55	8876
10	$9250 - 10000$	50	9611
11	$10000 - 12500$	56	11 032
12	$12500 - 15000$	26	13 572
13	$15000 - 17500$	16	16 162
14	> 17500	18	23 349

Table 4.2: Table of the energy bin incidence distribution of run 0499, with capacitors, showing the number of incidences and average charge absorption in the energy bins.

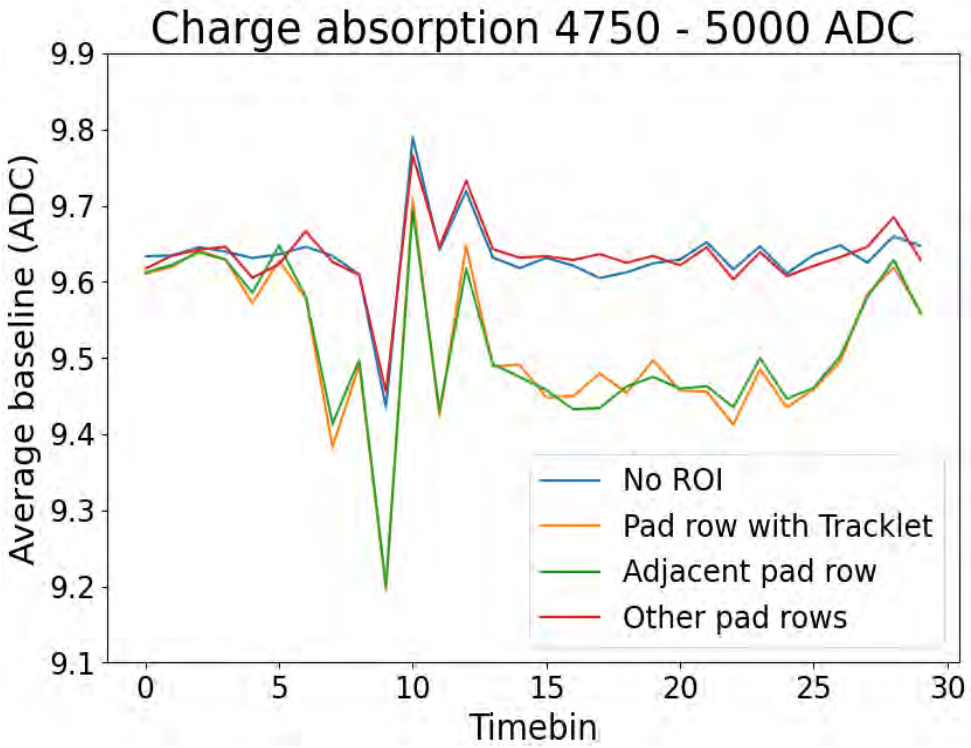

Figure 4.9: The shift in baseline due to charge absorption q of $4750 - 5500$ ADC, average charge absorption is 5103 AU, the average shift in the baseline across all time bins between the pad row of tracklet and event of no tracklet is 0.1203.

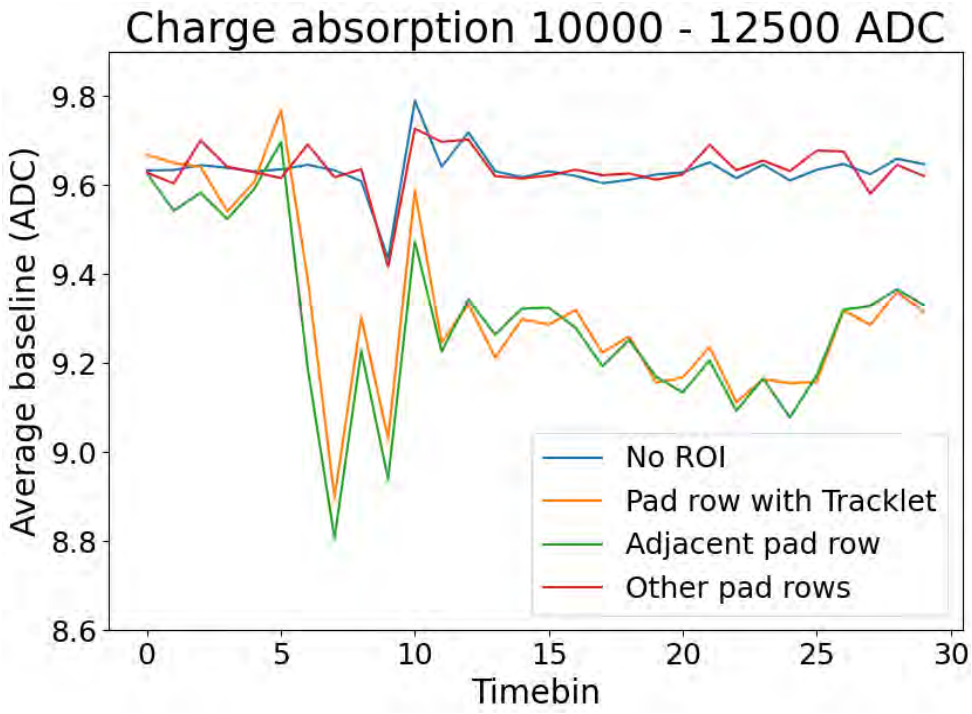

Figure 4.10: The shift in baseline due to charge absorption q of $10000 - 12500$ ADC, the average shift in the baseline across all time bins between the pad row of tracklet and event of no tracklet is 0.3101.

From figures 4.9 and 4.10 above, it is clear that the pad row of the tracklet and the adjacent pad row, with the same high voltage supply, both experience the shift in baseline equally, furthermore, the more charge absorbed, the larger the shift in baseline. The fluctuations at time bin 5 can be attributed to the trigger signal that induces a small signal once it arrives at the chamber, this effect is seen throughout the detector for all events. The average baseline of the pad rows with a tracklet for all the energy bins is plotted in figure 4.11 for a comparison.

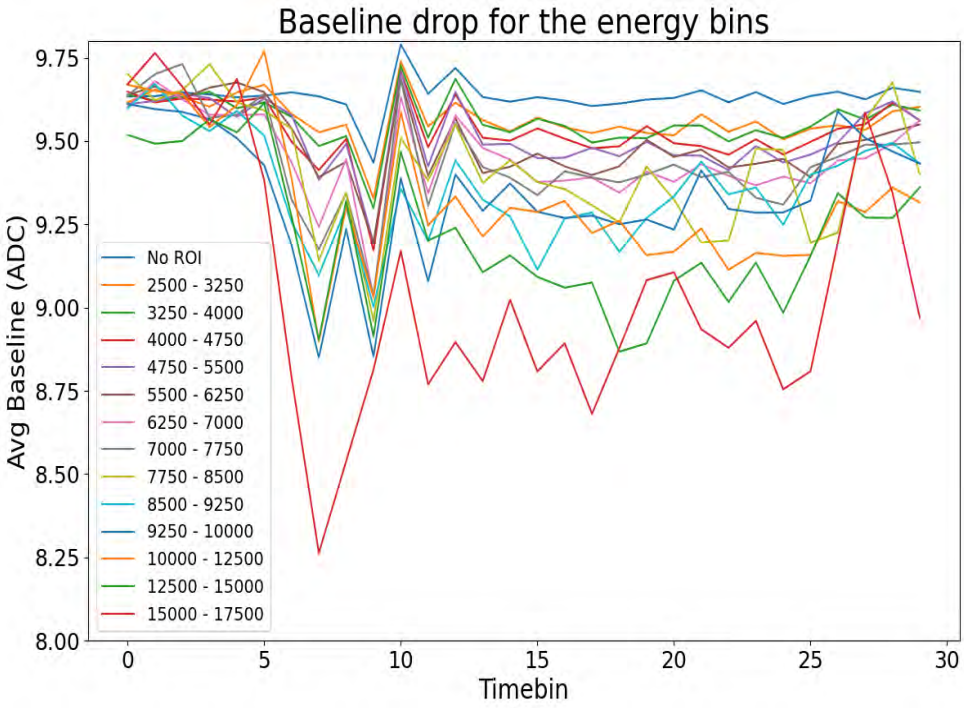

Figure 4.11: Shift in baseline as a function of time for the varying energy bins. Only the pad rows of tracklet interaction are shown.

Tabulating the above information, the baseline shift, given as the average baseline for No ROI minus the average baseline for the various energy bins, would be:

Energy bin	Energy range	Avg Charge Absorption	Avg baseline shift
1	2500 – 3250	2917	0.0673
2	3250 – 4000	3632	0.0742
3	4000 – 4750	4374	0.1035
4	4750 – 5500	5103	0.1203
5	5500 – 6250	5854	0.1387
6	6250 – 7000	6577	0.1851
7	7000 – 7750	7367	0.1931
8	7750 – 8500	8063	0.2137
9	8500 – 9250	8876	0.2743
10	9250 – 10000	9611	0.2961
11	10000 – 12500	11 032	0.3101
12	12500 – 15000	13 572	0.4159
13	15000 – 17500	16 162	0.5790

Table 4.3: Tabulated summary of the baseline shift and its dependence on absorbed charge - With capacitors.

Catering for the average in an energy bin, figure 4.12 below graphically shows the baseline drop and its dependence on charge absorption.

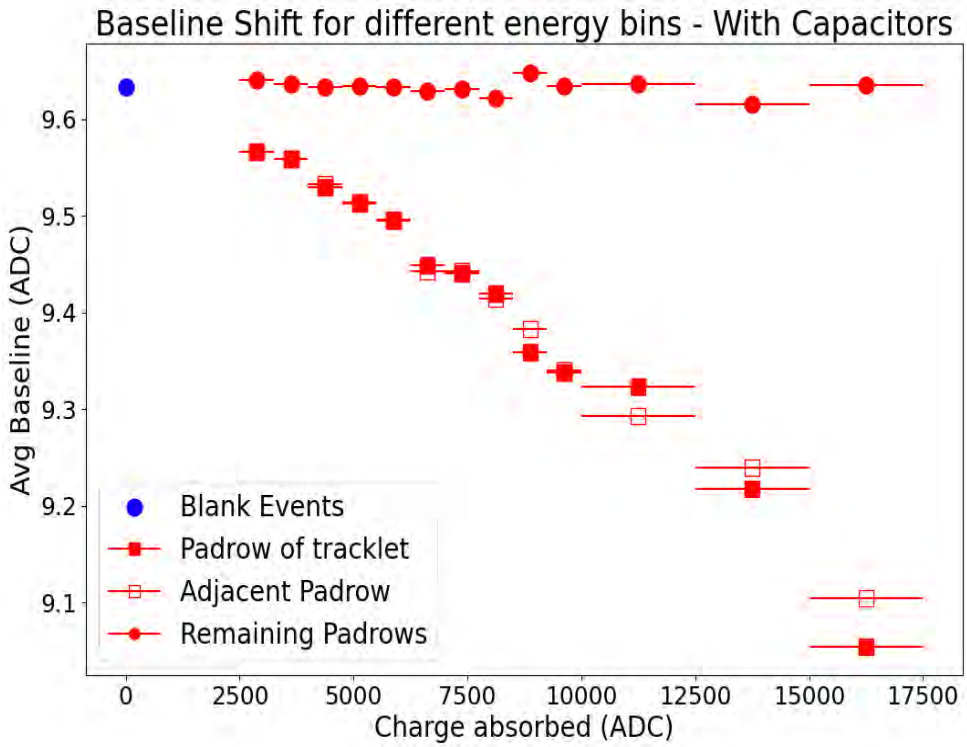

Figure 4.12: Overview of the shift in baseline for run 0499 as a function of charge absorbed. The blue dot (Blank Events) represents the average baseline across all time bins and events with no tracklets..

Note, for figure 4.12 above, the bar markers are placed within the center of the energy bin, and not the mean of the energy bin, as is given in table 4.3. The Blank events represents the average baseline across all time bins and events with no tracklets, giving a statistical representation of the average baseline of the detector chamber when there is no tracklet.

4.2.2 Without Capacitors - Run 0518

Following the same method as the run 0499 (with capacitors), run 0518 (without capacitors), is also NZ suppressed for 10,000 events. Below is figure 4.13 which shows the average energy distribution across the run.

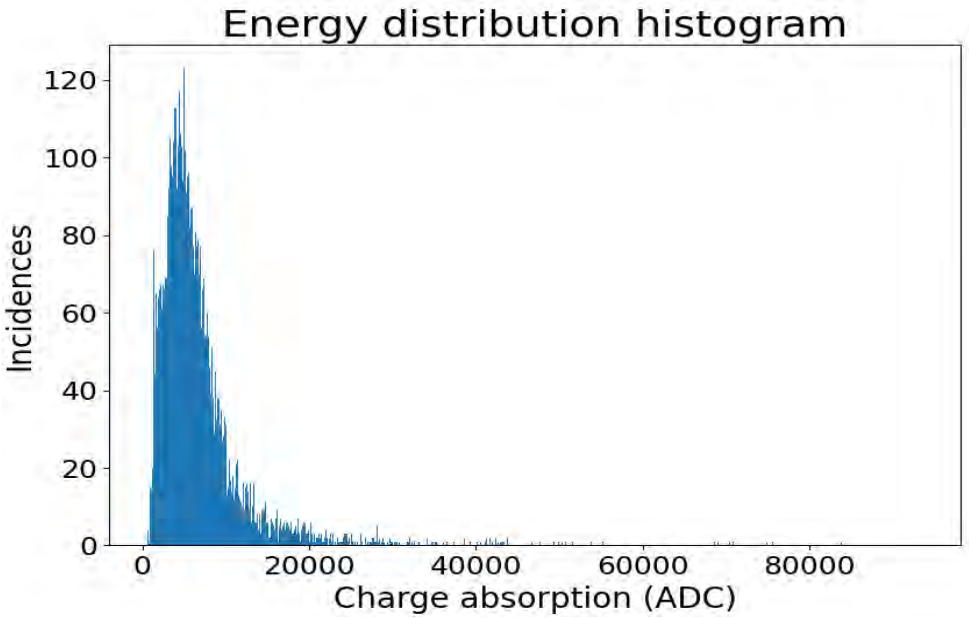

Figure 4.13: Energy Distribution histogram of run 0518. The peak with the highest number of incidence, 123, centres on 4992 AU.

A bin size of 94 is used in figure 4.13, hence all ADC values in a specific, discrete range in steps of 94, are grouped into a single bin, 1000 bins were used. Thus, for the point of highest incidence (123 counts), the energy range is 4992 ± 47 ADC values. With an anode voltage of 1600V and drift voltage of 2000V. The pulse height plot of the run is:

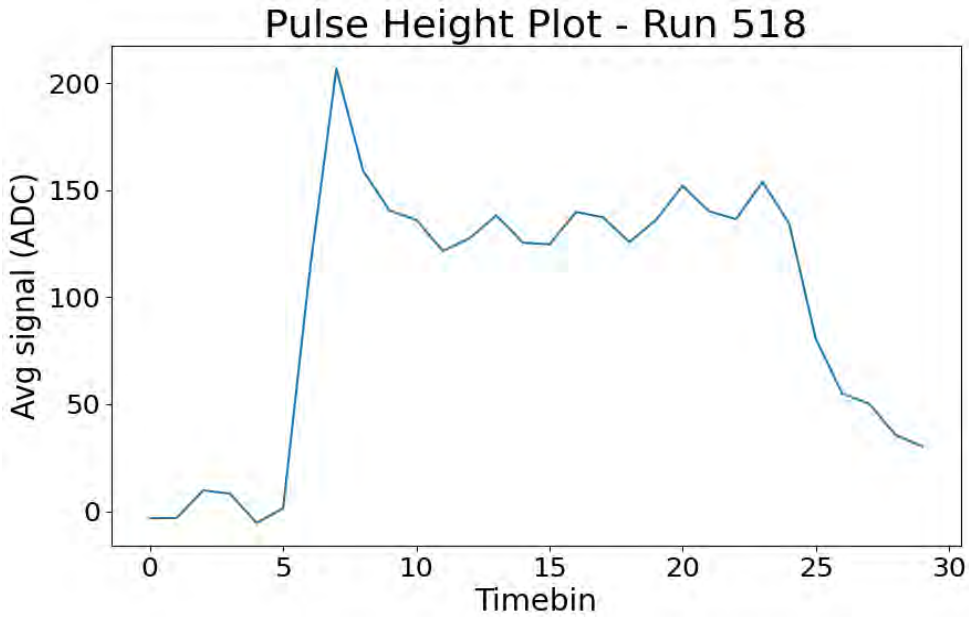

Figure 4.14: The Pulse Height Spectrum of run 0518, showing the average signal pulse as a function of time, which plateaus around 140 ADC.

With the visualisation of the energy distribution of the run, the regions of interest are then defined, using the same method as described in figure 4.2 above and its subsequent paragraph.

With the regions of interest isolated, below is table 4.4, where the details of the energy binning within the run are outlined.

Bin	Energy range (ADC)	Incidences	Avg charge absorption q (ADC)
0	< 2500	172	1848
1	$2500 - 3250$	195	2902
2	$3250 - 4000$	373	3648
3	$4000 - 4750$	451	4386
4	$4750 - 5500$	508	5130
5	$5500 - 6250$	445	5868
6	$6250 - 7000$	367	6626
7	$7000 - 7750$	291	7375
8	$7750 - 8500$	231	8123
9	$8500 - 9250$	163	8880
10	$9250 - 10000$	145	9580
11	$10000 - 12500$	214	11 048
12	$12500 - 15000$	85	13 709
13	$15000 - 17500$	50	16 313
14	> 17500	65	24 279

Table 4.4: Table of the energy bin statistical distribution of run 0518, without capacitors.

Table 4.4 shows the average tracklet energy signal for the different energy bins, once again, for values of 17500 ADC and larger, there is a small number of incidences spread across a very large energy range and thus produces no statistical significance, hence has been omitted, as can be seen on figure 4.13.

Once again, the relationship of the baseline of each energy bin is compared for the 3 sectors (pad row of tracklet, adjacent pad row and the average of the remaining pad rows within the event). Two examples of these are shown below.

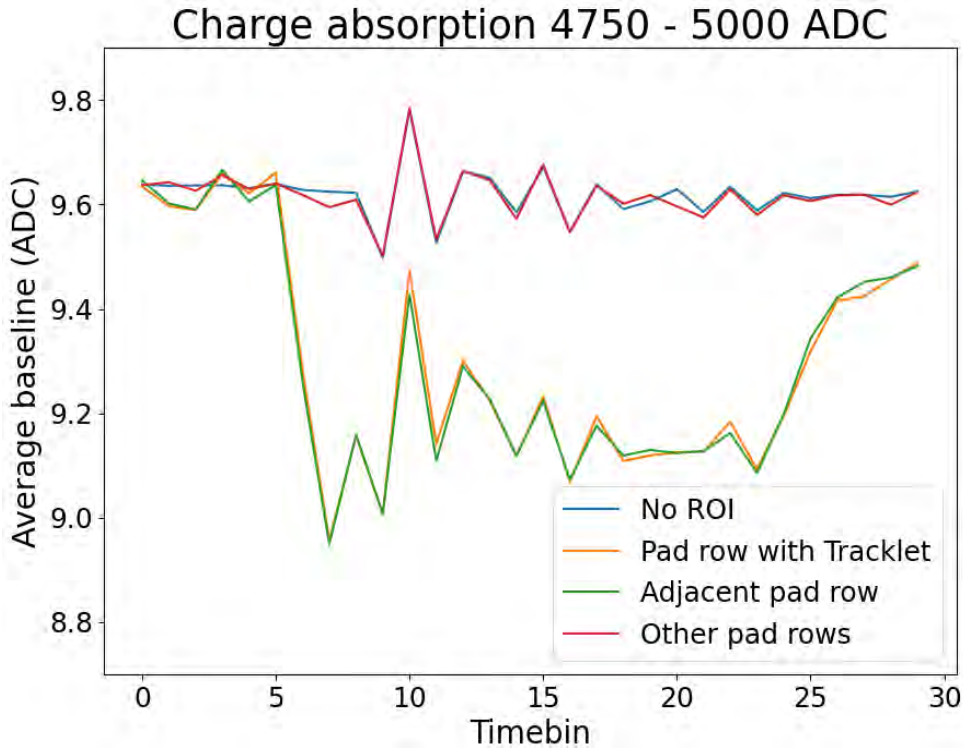

Figure 4.15: The shift in baseline due to charge absorption q of $4750-5500$ ADC, average energy absorption is 5130 AU, the average shift in the baseline across all time bins between the pad row of tracklet and event of no tracklet is 0.3208.

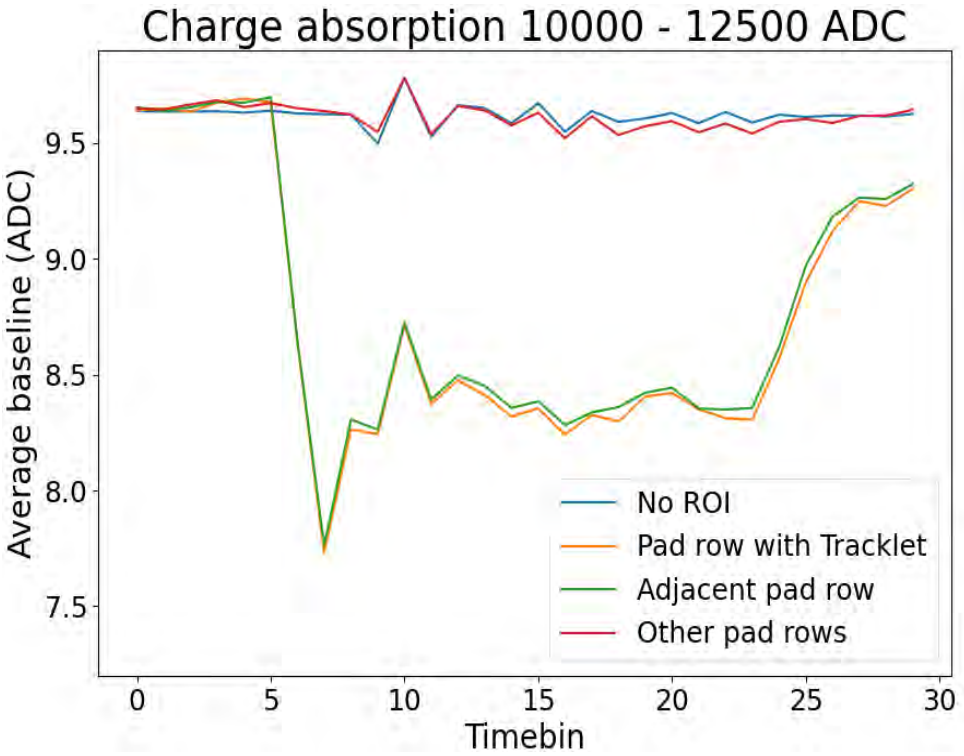

Figure 4.16: The shift in baseline due to charge absorption q of $10000-12500$ ADC, average energy absorption is 11 048 AU, the average shift in the baseline across all time bins between the pad row of tracklet and event of no tracklet is 0.8695 ADC counts.

From figure 4.15 and 4.16 above, just as with the case of run 0499, the pad row of the tracklet and the adjacent pad row, with the same high voltage supply, both experience the shift in baseline equally, with a direct relationship between the drop in baseline and the amount of charge absorbed. Figure 4.17 below summarises the shift for different energies for the tracklet pad rows.

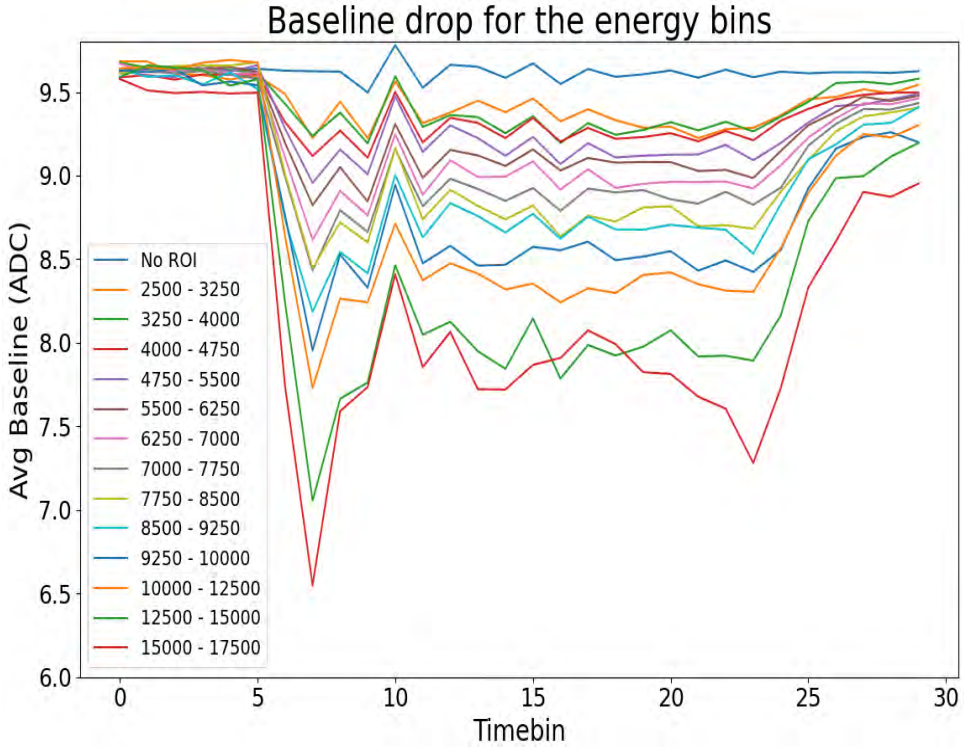

Figure 4.17: Shift in baseline as a function of time for the different energy bins on run 0518. Only the pad rows of tracklet interaction are shown.

Tabulating the above data:

Energy bin	Energy range	Avg charge absorption	Avg baseline shift
1	2500 – 3250	2902	0.1887
2	3250 – 4000	3648	0.2023
3	4000 – 4750	4386	0.2579
4	4750 – 5500	5130	0.3208
5	5500 – 6250	5868	0.3805
6	6250 – 7000	6626	0.4511
7	7000 – 7750	7375	0.5266
8	7750 – 8500	8123	0.5837
9	8500 – 9250	8880	0.6689
10	9250 – 10000	9580	0.7865
11	10000 – 12500	11 048	0.8695
12	12500 – 15000	13 709	1.1664
13	15000 – 17500	16 313	1.3566

Table 4.5: Tabulated summary of the average baseline shift and its dependence on energy - Without capacitors.

With the data of run 0518 (without capacitors) rendered as a function of energy, figure 4.18 below shows the baseline shift plotted as a function of energy.

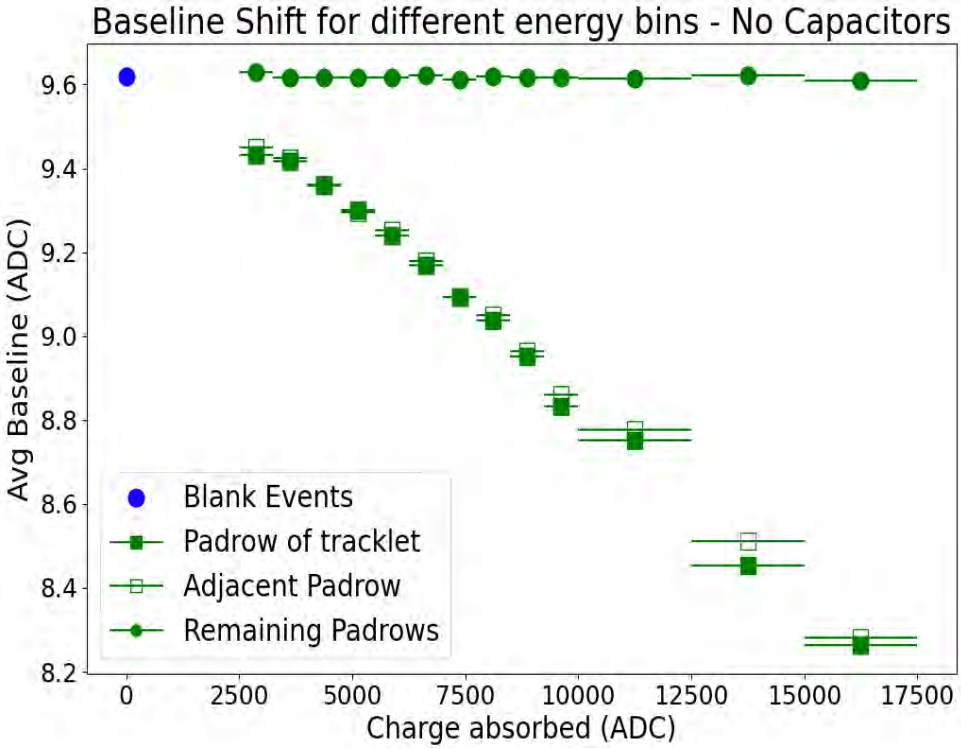

Figure 4.18: Summary of the shift in baseline of run 0518, as a function of charge absorption.

Note, for figure 4.18, as is with the case of figure 4.12, the bar markers are placed within the center of the energy bin, and not the mean of the energy bin as given in table 4.5.

4.2.3 Comparison

The results can then be set side by side for comparison, giving:

Energy bin	Energy range	q 0499	q 0518	Avg BlS 0499	Avg BlS 0518
1	2500 – 3250	2917	2902	0.0673	0.1887
2	3250 – 4000	3632	3648	0.0742	0.2023
3	4000 – 4750	4374	4386	0.1035	0.2579
4	4750 – 5500	5103	5130	0.1203	0.3208
5	5500 – 6250	5854	5868	0.1387	0.3805
6	6250 – 7000	6577	6626	0.1851	0.4511
7	7000 – 7750	7367	7375	0.1931	0.5266
8	7750 – 8500	8063	8123	0.2137	0.5837
9	8500 – 9250	8876	8880	0.2743	0.6689
10	9250 – 10000	9611	9580	0.2961	0.7865
11	10000 – 12500	11 032	11 048	0.3101	0.8695
12	12500 – 15000	13 572	13 709	0.4159	1.1664
13	15000 – 17500	16 162	16 313	0.5790	1.3566

Table 4.6: Tabulation of the data runs, 0499 - With capacitors and 0518 - Without capacitors. q signifies the average charge absorption in that energy bin and BlS is the baseline shift in that energy bin.

Graphically:

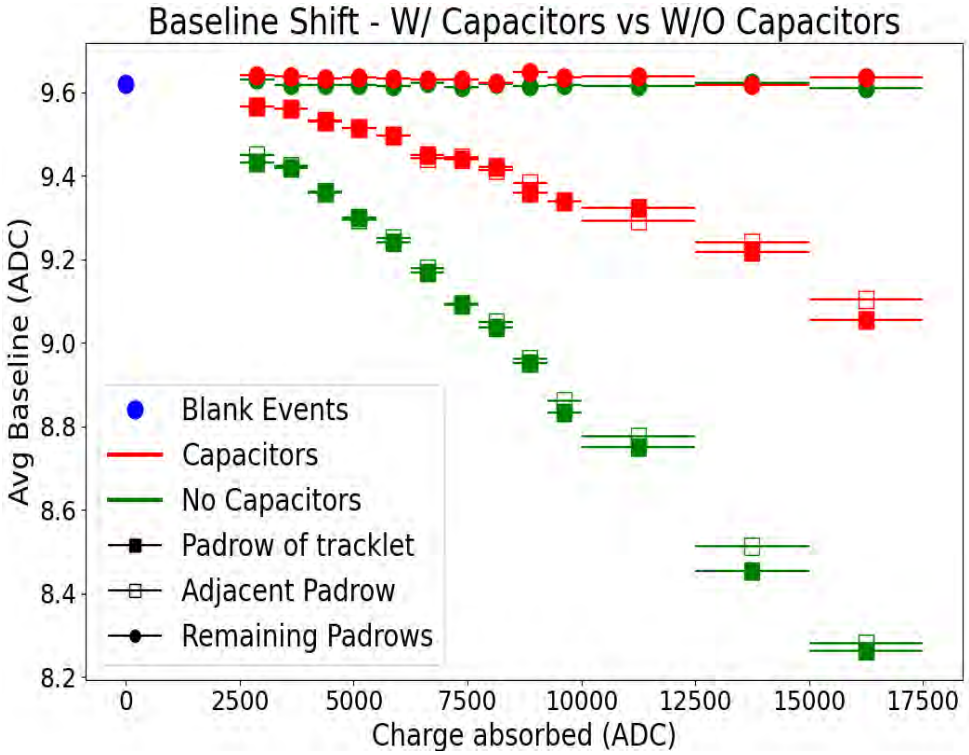

Figure 4.19: Summary and comparison of runs, with and without capacitors.

Note, for figure 4.19, same as with figure 4.12 and 4.18, the icons represent the centre of the bin, and not the weighted mean within the bin, as given in table 4.6. Further detailed analysis to be followed in section 4.3.

4.3 Results

Within the TRD chamber, there is a marginally large and clear baseline shift due to removing the capacitors, this effect is dependent on the amount of charge absorbed by the anode wires. This effect is also only confined to the pad row where the tracklet traversed, as well as the adjoining pad row with the same high voltage supply. There is no effect on the remaining pad rows within the chamber.

To further investigate the effects in question, the baseline as a function of charge absorbed in the 2 runs (figures 4.18 and 4.12) is plotted with the center of the energy bin, not the weighted mean of the energy bin. The data was plotted as a scatter plotted with the weighted mean and uncertainties included to visualise a relationship:

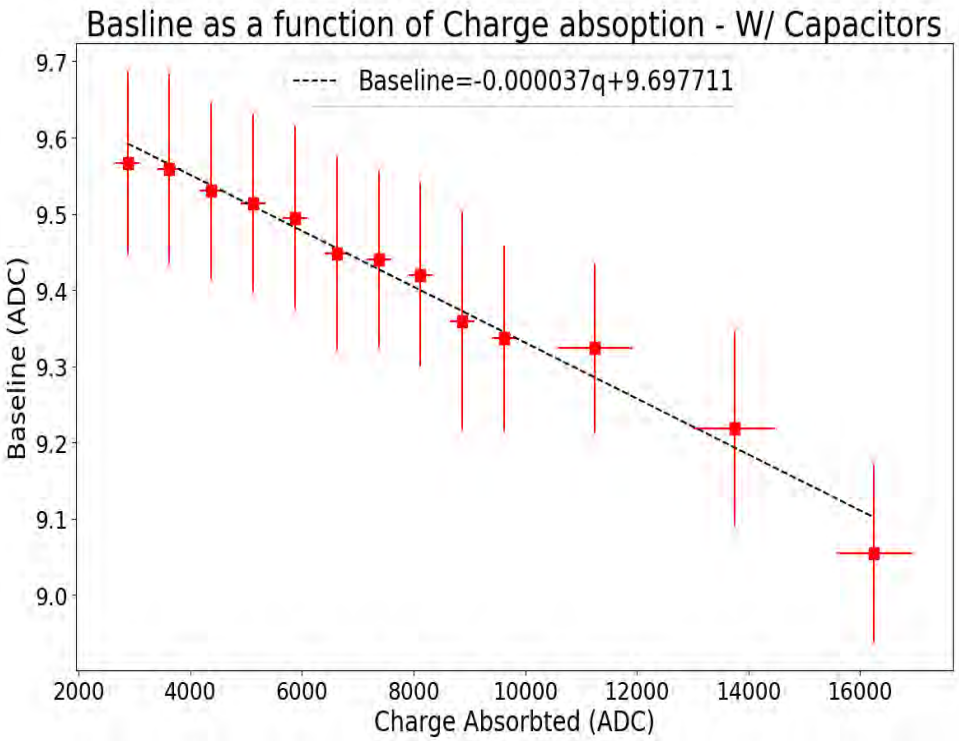

Figure 4.20: Linearity visualisation of the drop in baseline for run 0499, the x values show the weighted mean of the energy bins. The linearisation gives the relationship where the baseline can be approximated by $\mathrm{BL} = 9.697 - 3.723 \times 10^{-5} q$.

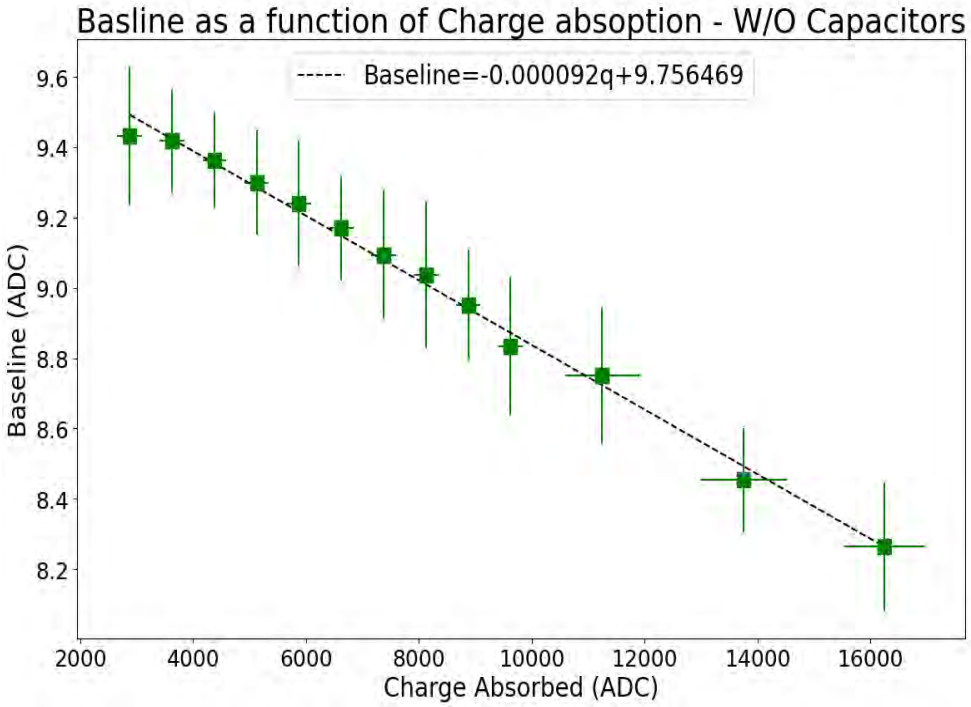

Figure 4.21: Linearity visualisation of the drop in baseline for run 0518 - Without capacitors, the x values show the weighted mean of the energy bins. The linearisation gives the relationship where the baseline can be approximated by $\mathrm{BL} = 9.756 - 9.225 \times 10^{-5} q$.

Run 0517 - without capacitors, was also analysed to verify the results of run 0518, as well as give an indication of the effect a different anode voltage may produce.

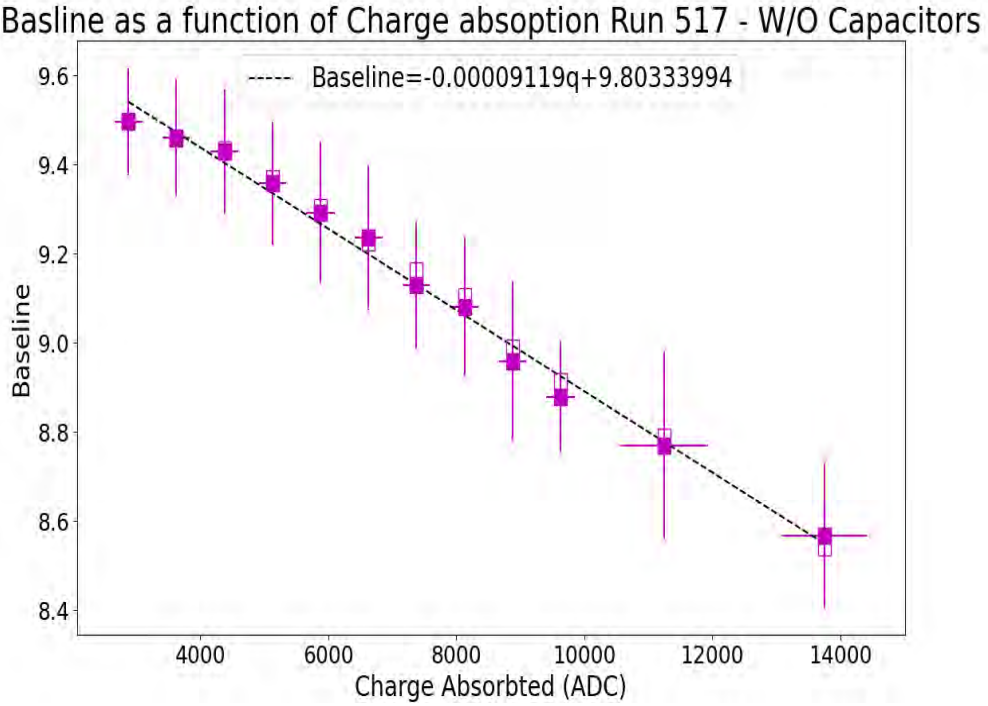

Figure 4.22: Linearity visualisation of the drop in baseline for run 0517 - Without capacitors. The linearisation gives the relationship where the baseline can be approximated by $\mathrm{BL} = 9.803 - 9.119 \times 10^{-5} q$.

The uncertainty along the baseline for a specific energy bin is a projection of the inherent fluctuations within the pads of the TRD chamber. These fluctuations can be seen in figure 4.23. A deeper explanation is outside the scope of this dissertation.

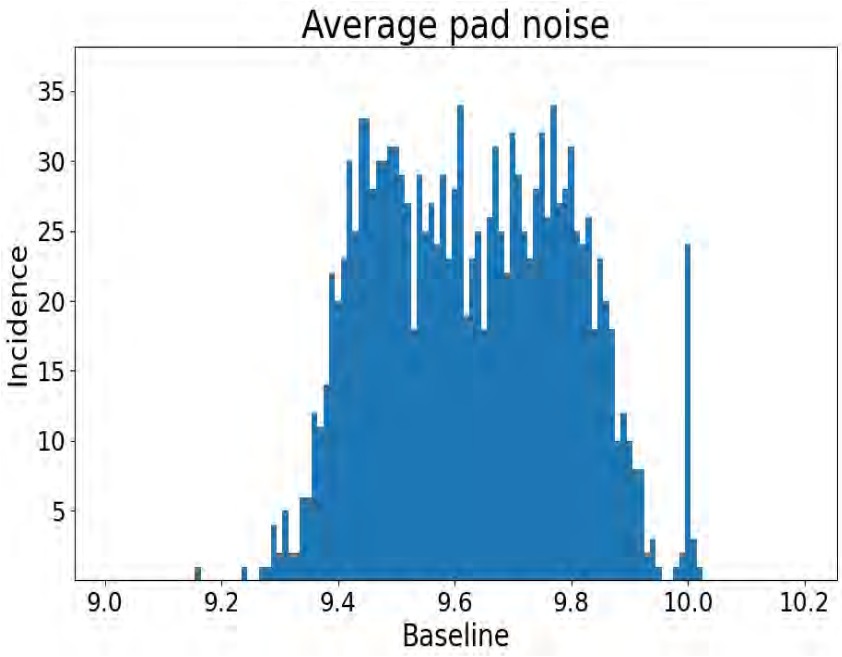

Figure 4.23: Distribution of the average noise contribution per pad for an entire run, an incidence refers to a single pad, which gives the average over the 30 time bins across all events without tracklets, there is a total of 1776 incidences. The average baseline is 9.632 ± 0.164 .

With figure 4.23 above, beside the drop of the baseline due to charge absorption from the tracklet, there is also the fluctuation in noise by the pads themselves. For this figure, the average baseline is 9.632, with a standard deviation of 0.164, which is on par with the fluctuations around the baseline of runs 0499 and 0518. Thus, this fluctuation contributes (severely) to the baseline uncertainty per energy bin in figures 4.20 and 4.21.

Following figures 4.20 and 4.21, where the gradient of the graph gives the relationship between the shift in baseline and the amount of charge absorbed, the uncertainty within these plots is determined.

For run 0499, with capacitors, the slope, along with its uncertainty, is given as:

$$m_{0499} = -3.723 \times 10^{-5} \pm 0.162 \times 10^{-5}$$

For run 0518, without capacitors, the slope, along with its uncertainty, is given as:

$$m_{0518} = -9.225 \times 10^{-5} \pm 0.214 \times 10^{-5}$$

Giving errors due to uncertainty of:

$$\frac{3.723 \times 10^{-5}}{0.162 \times 10^{-5}} = 4.34\% \quad \text{and} \quad \frac{9.225 \times 10^{-5}}{0.214 \times 10^{-5}} = 2.32\%$$

for run 0499 and 0518 respectively.
For the constants on figures 4.20 and 4.21, the uncertainty is:

$$9.698 \pm 0.014 \quad \text{and} \quad 9.756 \pm 0.019$$

for runs 0499 and 0518 respectively. Giving errors due to uncertainty of:

$$\frac{0.014}{9.698} = 0.14\% \quad \text{and} \quad \frac{0.019}{9.756} = 0.19\%$$

for runs 0499 and 0518 respectively.

Thus, the relationship giving the overall linearity between the baseline and the amount of charge absorbed, from data with a capacitor and without, is:

$$BL_{0499} = (9.698 \pm 0.014) - (3.723 \pm 0.162) \times 10^{-5}\ q$$

and

$$BL_{0518} = (9.756 \pm 0.019) - (9.225 \pm 0.214) \times 10^{-5}\ q$$

With a known capacitance removed, the inherent capacitance can be calculated. Considering the overall factor drop of:

$$\frac{m_{0518}}{m_{0499}} = \frac{9.225 \times 10^{-5}(\pm 2.32\%)}{3.723 \times 10^{-5}(\pm 4.34\%)} = 2.478 \pm 6.66\% = 2.478 \pm 0.165$$

This shows that, for the same amount of charge absorbed, there is a $2.478(\pm 0.165)$ times larger drop in the baseline without capacitors, as compared to the baseline with the 2.2 nF capacitors. Hence, the inherent/parasitic capacitance of the system is:

$$2.478(\pm 0.165) \times C_{Inh} = 2.2 \text{ nF} + C_{Inh}$$

$$1.478 C_{Inh} = 2.2 \text{ nF}$$

$$C_{Inh} = 1.489 \pm 0.075 \text{ nF}$$

Which correlates to a 5% uncertainty on the inherent capacitance.
Applying equation 3.6 to the L3C0 chamber at the University of Cape Town, with specifications of:

$h_{cp} \equiv$ Distance between the anode wire and the cathode wire plane below = 3.5 mm

$h_{pp} \equiv$ Distance between center of wire and pad plane = 3.5 mm

$a \equiv$ Radius of the wire = 0.255 mm

$L \equiv$ The length of the wire = 900 mm

$h_{ww} \equiv$ Distance between each anode wire = 5 mm

$n \equiv$ Number of wires per pad row pair = 34

This information, substituted in equation 3.6, gives:

$$C = \frac{2\pi\epsilon_0(900 \times 10^{-3})}{\ln\left(\frac{3.5\times10^{-3}}{0.255\times10^{-3}} + \sqrt{\left(\frac{3.5\times10^{-3}}{0.255\times10^{-3}}\right)^2 - 1}\right)}$$

Thus, the inherent capacitance between a single wire and the pad plane is:

$$C_{aw} = 15.1 \text{ pF} \quad \text{per anode wire}$$

For a pad row pair:

$$C_{pp} = 15.1 \text{ pF} \times n = 15.1 \text{ pF} \times 34 = 513.4 \text{ pF} \quad \text{per pad row pair}$$

Considering the cathode wire lining beneath, spaced the same distance from the anode wires as the pad plane is from the anode wires, it doubles the effect of capacitance:

$$C_{pp,gp,cp} = 513.4 \text{ pF} \times 2 = 1026.8 \text{ pF} = 1.027 \text{ nF} \quad \text{for a pad row pair}$$

Applying equation 3.7 to the same specifications, the capacitance between two anode wires would would be:

$$C = \frac{\pi\epsilon(900 \times 10^{-3})}{\ln\left(\frac{5\times10^{-3}}{0.255\times10^{-3}}\right)} = 8.408 \text{ pF}$$

For each pad row pair:

$$C_{ww,pp} = 8.408\ pF \times 34 = 0.286 \text{ nF}$$

Thus, the total calculated inherent capacitance, for a pad row pair, is:

$$C_{Total} = C_{pp,gp,cp} + C_{ww,pp} = 1.027 \text{ nF} + 0.286 \text{ nF} = 1.313 \text{ nF}$$

The above experimentally calculated inherent capacitance, 1.313 nF, differs from the mathematically calculated value, 1.489($\pm$0.075) nF, by 0.176 nF.
The above conforms within 3 sigma, with other contributors to uncertainty not included, such as the accuracy of the variables used in the equation, as well as mechanical shifts within the chamber (separation between wires, as well as the distance of the wires from the pad plane and cathode wire plane). There is insulation around the anode wires, which would drop the capacitance of the wires. The fluctuations in voltage, though minute, can contribute to a difference. Capacitance between the wires is only considered for the immediate wires within the two pad rows of interest, there is, however, influence from the wires outside these pad rows on the wires at the edge of the pad rows. The cathode wires are also considered as planes, though they are individual wires spaced 2.5 mm apart. Inherent capacitance exists due to the proximity of one electrical component to another, any component within proximity to the anode wire, with a different voltage, contributes to the inherent capacitance.

For a worst case scenario, considering a head on Pb-Pb collision, the maximum charge deposition averaged to be:

$$\frac{63000}{5} \cdot 27.3 = 343980 \text{ ADC counts}$$

The above is the total average absorbed charge within the entire chamber, assuming a 16 pad row chamber, giving 8 pad row pairs:

$$\frac{343980}{8} = 43000 \text{ ADC counts per pad row pair}$$

Therefore, with the worst case scenario of charge deposition in a voltage segment of 43 000 ADC counts, the baseline at the UCT TRD chamber would be:

$$\text{BL}_{Pb-Pb} = 9.756 - 9.225 \times 10^{-5} \times 43000 = 5.789$$

With the given worst case scenario, the lowest baseline of the chamber at a given high voltage segment is 5.789, a baseline drop of 3.843.

Allowing for 2σ on the baseline, where each sigma corresponds to the directional fluctuation of 1.2 ADC counts, 2σ would correlate to 2.4 ADC counts. In this case, the baseline would be 9.632 - 2.4 = 7.2 ADC counts. A charge absorption of 43 000 ADC counts in a high voltage segment would put the baseline at 3.3 ADC counts. For reference, with the allowance of 2σ for the baseline, the amount of charge absorption in a high voltage segment to drop the baseline to 0 would be 79 769 $\approx$ 80 000 ADC counts.

To correct for the baseline of the surrounding pads, the pads remaining within the pad rows that were not involved in the interaction and those at the adjacent pad row experience this common mode effect, the value deducted as a function of charge absorbed, should be added on once more. Therefore:

$$\mathrm{BL}_{corrected} = \mathrm{BL} + 9.225 \times 10^{-5}\ q \tag{4.1}$$

The above, applied for all pads in the pad row with tracklet, excluding the pads that partook in the interaction, and the adjacent pad row, would correct for the baseline. Implementing this and plotting it, the results are:

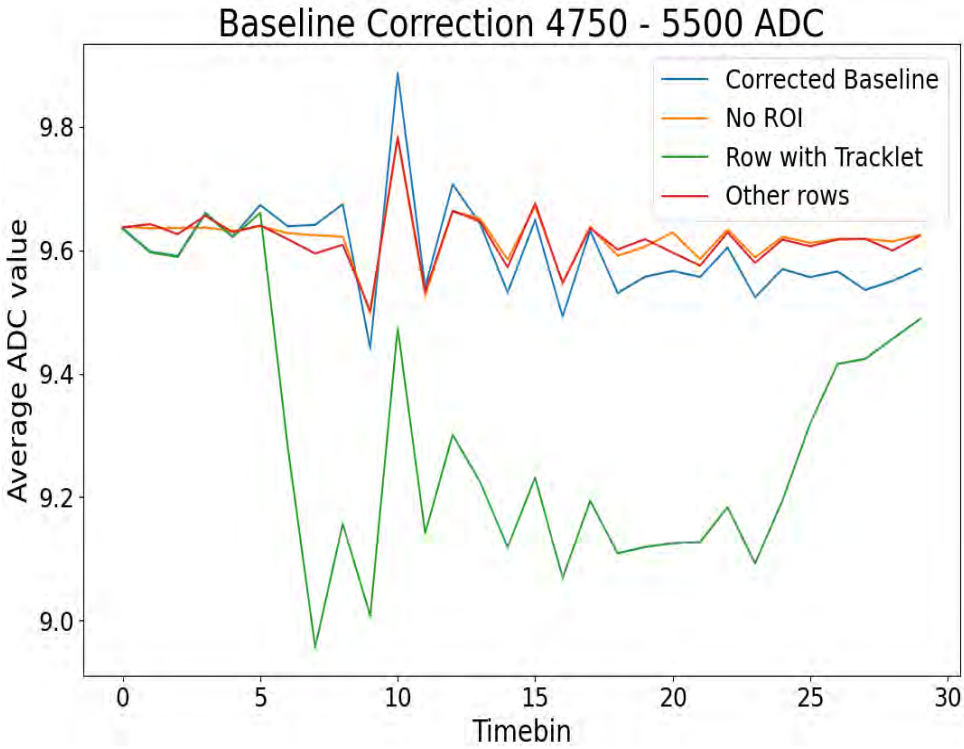

Figure 4.24: The corrected baseline for bin 4 (4 750 - 5 500 ADC) of run 0518 - Without capacitors, as a function of time. The average baseline across the corrected pad row is 9.598.

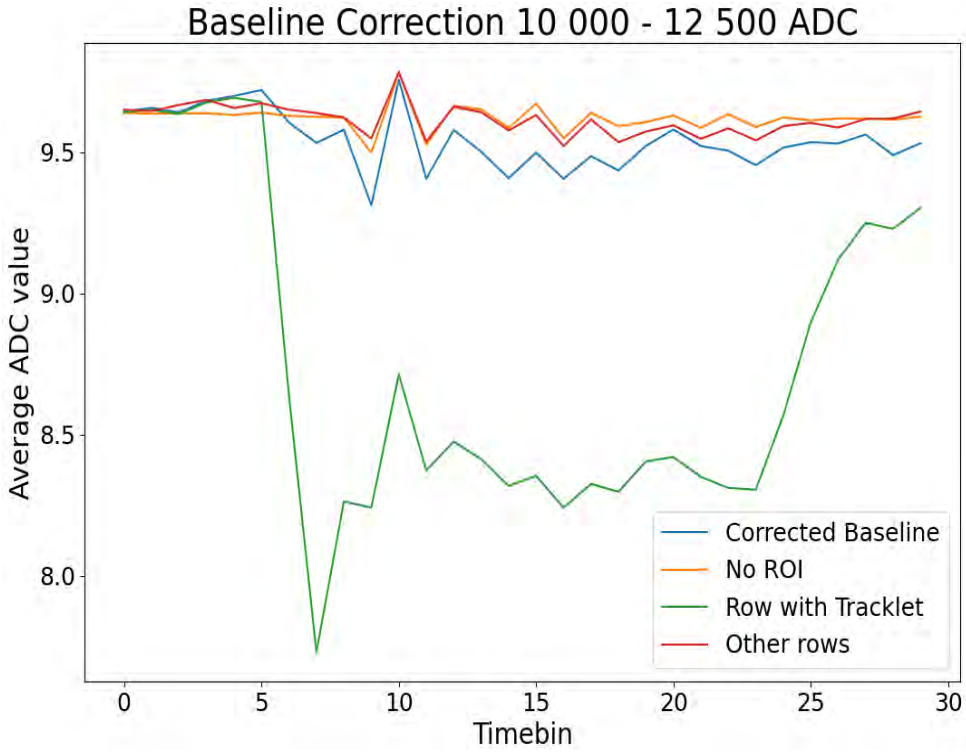

Figure 4.25: The corrected baseline for bin 11 (10 000 - 12 500 ADC) of run 0518 - Without capacitors, as a function of time. The average baseline across the corrected pad row is 9.543.

Figures 4.24 and 4.25 above give the corrected baseline on a time bin basis for all events in a specific energy bin. Essentially, figures 4.24 and 4.25 are figures 4.15 and 4.16 corrected using equation 4.1. The corrected average baseline of 9.598 and 9.543 fall within 1 σ of the no tracklet average baseline of 9.632 $\pm$ 0.164.

Chapter 5

Conclusion

The primary aim of this research was to determine the shift in the baseline and extent of the common mode effect when the capacitors are removed from the chambers of the ALICE Transition Radiation Detector, then correcting for it. A comparison of the baseline shifts is done between two different runs, with the same high voltage settings for the drift (2000 V) and anode (1600 V) voltages, but one run with capacitors installed and another without capacitors installed, run 0517 with and anode voltage of 1500 V and drift voltage of 2000 V was also analysed to compare the effects of the anode voltage on the results. The baseline is defined as the average ADC value of the pads when there is no charge absorption, the common mode effect is the effect experienced by pads in the vicinity of a tracklet path. Hence, when a tracklet traverses a specific pad row in a chamber, a common mode effect is experienced by the surrounding pads that cause a drop in baseline proportional to the amount of charge absorbed.

The analysis project first managed to discern that the baseline shift experienced by pads when charge is absorbed, is limited to the pads within the pad row of interaction, as well as the adjoining pad row, which is the pad row with the same high voltage supply. No other pad rows are affected.

The relationship between the baseline and the amount of charge absorbed for the run without capacitors, is:

$$BL_{woc} = (9.756) - 9.225 \times 10^{-5}\ q$$

While for the run with capacitors, is:

$$BL_{wc} = (9.698) - 3.723 \times 10^{-5}\ q$$

Where q is the amount of charge absorbed by the anode wires.

This experiment has found that there is a drop in baseline 2.478 ± 0.165 larger on the run without capacitors compared to that with capacitors, for the same amount of charge absorbed. With the relationship above, the run without capacitors suggests an upper charge absorption limit of 80 000 ADC counts when the baseline is considered to be 2σ from the average (below). An estimated charge absorption of 343 000 ADC counts has been considered as the worst case scenario in a central Pb-Pb collision and would be experienced across the entire chamber, giving an average of 43 000 ADC counts per high voltage segment.

For the L3C0 Read Out Chamber located at the University of Cape Town, the average baseline of the chamber, without capacitors, is determined to be 9.632 ± 0.164.

Upon further analysis of results, specifically higher energy absorption bins, if more than a single tracklet traverses a pad row pair in a single event, the sum of the charge absorbed can be applied to determine the baseline shift. Hence, within the same event and for a pad row pair, charge absorption affecting the baseline is additive. In addition, if two tracklets traverse the detector within the same event, but not on a pad row pair, there is no net effect on the other, and thus should be considered as isolated events and corrected for separately.

The baseline correction for the data can be written as:

$$BL_{corrected} = BL_{read} + 9.225 \times 10^{-5}\ q$$

Where q is the amount of charge absorbed.

Removal of the capacitors from the chambers of the ALICE TRD breaks the low pass filter (RC circuit). This in turn creates fluctuations within the voltage supply and creates a common mode effect that is 2.5 times larger in the data without capacitors.

Run 0517 - without capacitors which is run at the same parameters as run 0518, except with a lower anode voltage of 1500 V as opposed to 1600 V, gave a relationship between the baseline and charge absorption within one σ of the relationship of run 0518. This signifies that the contributor to the baseline shift is the amount of charge absorption. This, coupled with the evidence that the charge is additive, shows that the high tracklet counts at CERN can be mimicked by a system operating with a high gain.

The inherent capacitance of the L3C0 chamber is calculated as 1.489 ± 0.075 nF, while the calculated capacitance of the chamber is determined to be 1.313 nF, which conforms within 3σ.

Appendix A

With Capacitors

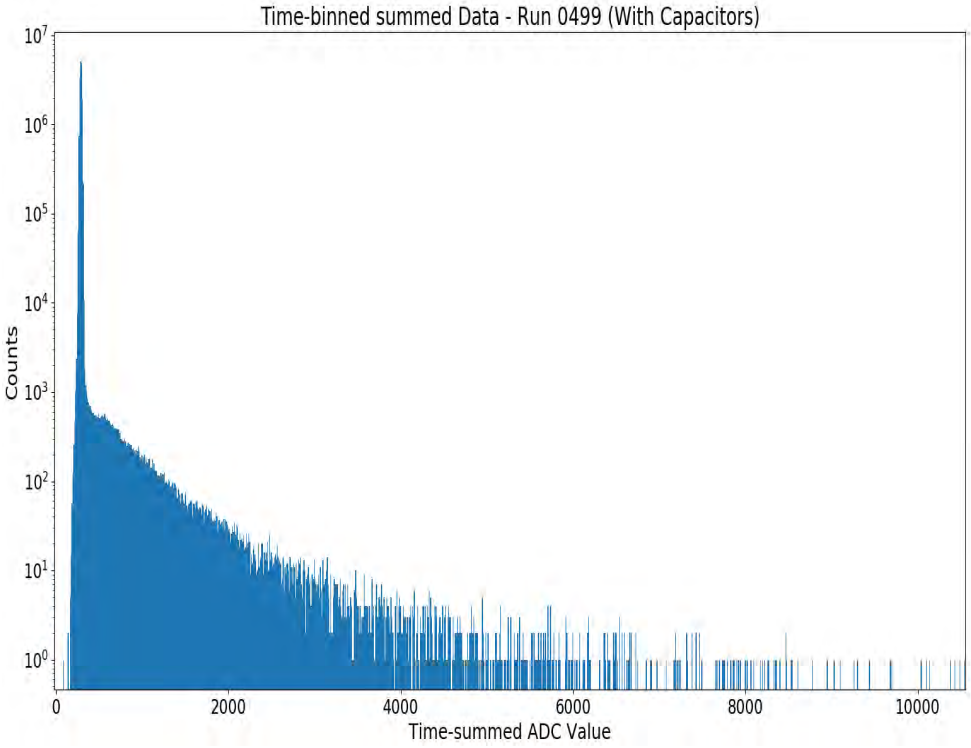

Figure A.1: The time-binned summed data for run 0499 - With capacitors. Peak is at 286 ADC values.

Appendix B

Without Capacitors

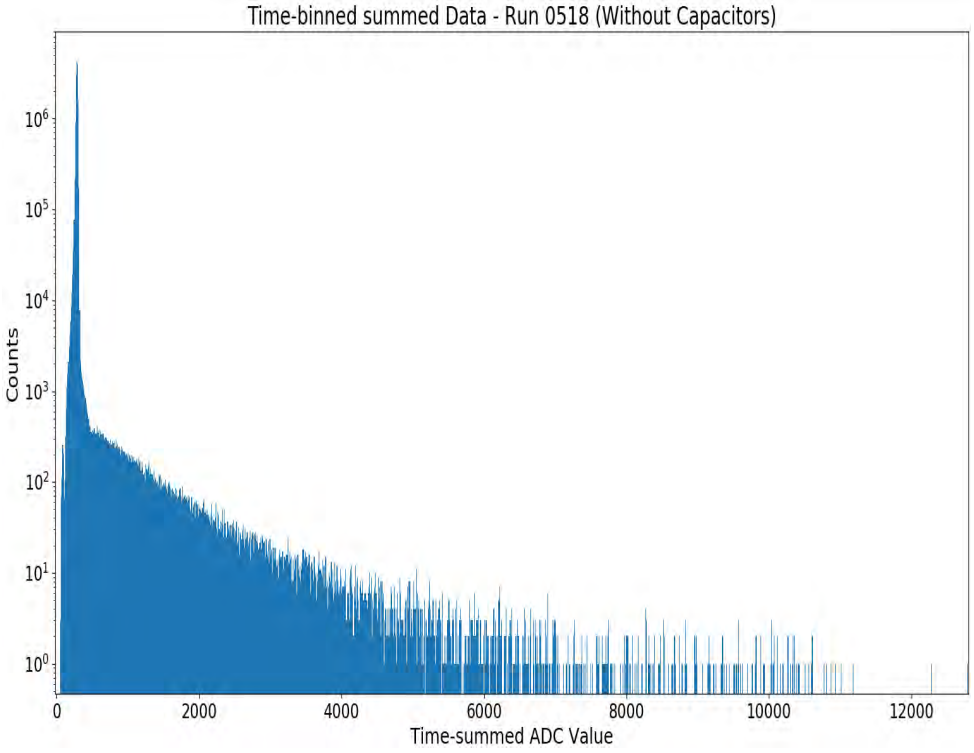

Figure B.1: The time-binned summed data for run 0518 - Without capacitors. Peak is at 288 ADC values.

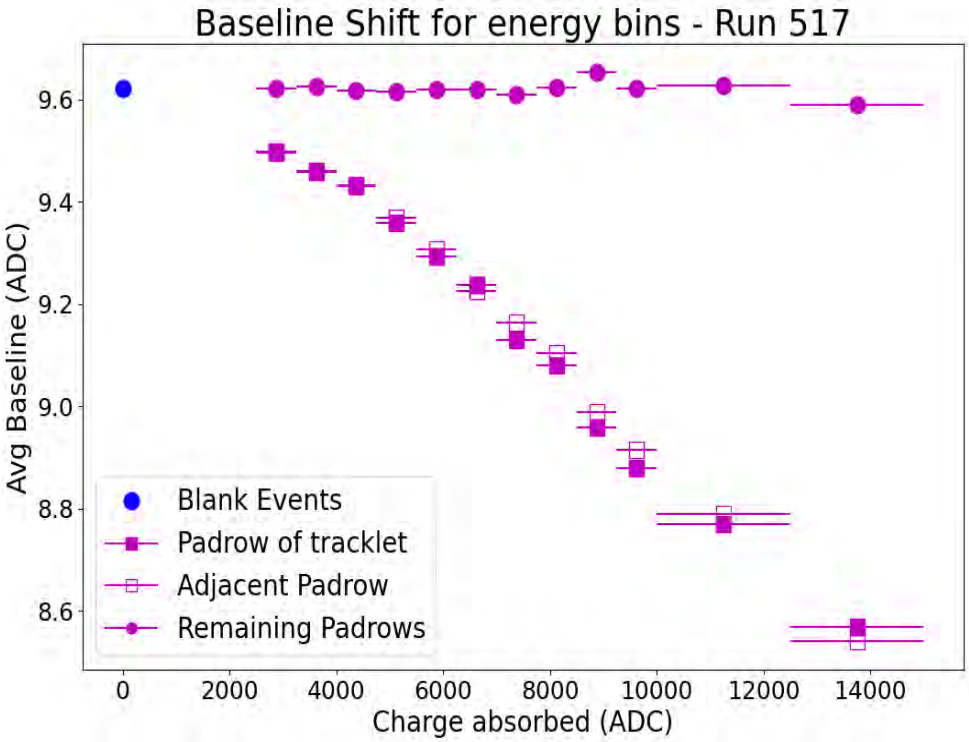

Figure B.2: Summary of the shift in baseline of run 0517 - Without capacitors, as a function of charge absorption.

Bibliography

[1] ALICE Collaboration, *ALICE Technical Design Report of the Transition Radiation Detector*. CERN Report, LHCC 2001-021, October 2001.

[2] F. Sauli, *Principles of Operation of Multi-wire Proportional and Drift Chambers*. CERN Report 77-09, 03 May 1977.

[3] Andrea Romanino, *The Standard Model of Particle Physics*. Article entry I - 34151 Trieste, SISSA Italy.

[4] Johannes Hendrik Stiller, *Gain Calibration of the ALICE TRD using the Decay of ^{83m}Kr and Alignment of the ALICE TRD*. PhD Thesis, University of Heidelberg, 2011.

[5] Christian Klein-Bosing, *TRD Status Report*. Presentation at ALICE week, IKP Munster, March 2019.

[6] K. Oyama, *Reference cross section measurement with ALICE in pp and Pb-Pb collisions at LHC*. Publication arXiv:1305.7044v1, University of Heidelberg, May 2013.

[7] Heidelberg University,
`http://ew-dev.physi.uni-heidelberg.de/~rubio/LogicBox/index.php/Main_Page`
Physics Institute of Heidelberg.

[8] H. Bichsel, D.E. Groom and S.R. Klein, *Passage of Particles Through Matter*, University of Washington PL B667, February 2010.

[9] ALICE Collaboration,
The ALICE Experiment at the CERN LHC JINST 3 S08002, 2008.

[10] Michael H. Seymour, *Quantum Chromodynamics*. CERN-PH-TH/2009-194, University of Manchester, October 2010.

[11] Anastasia Berdnikova, *Private Communication*, ALICE Collaboration.

[12] ALICE Collaboration, *Technical Design Report for the Upgrade of the ALICE Time Projection Chamber*. ALICE - TDR - 016, CERN, February 2015.

[13] ALICE Collaboration, *Technical Design Report for the Upgrade of the ALICE Inner Tracking System*. CERN - LHCC - 2013 - 024, November 2013.

[14] ALICE Collaboration, *ALICE Technical Design Report of the Time of Flight System*. CERN / LHCC 2000–12, CERN, February 2000.

[15] ALICE Collaboration, *Technical Design Report of the Photon Multiplicity Detector (PMD)*. CERN / LHCC 99–32, CERN, September 1999.

[16] ALICE Collaboration, *The ALICE Transition Radiation Detector: construction, operation and performance*. CERN-EP-2017-222, CERN, August 2017.

[17] ALICE Collaboration,
Technical Design Report for the Muon Forward Tracker. CERN-LHCC-2015-001, May 2015

[18] Fabio Schlichtmann, *Pressure and high-voltage calibration of the Alice Transition Radiation Detector*. University of Heildelberg, 2018.

[19] ALICE Collaboration, *ALICE Technical Design Report of the Photon Spectrometer*. CERN / LHCC 99–4, CERN, March 1999.

[20] David Emschermann, *Construction and Performance of the ALICE Transition Radiation Detector*. PhD Thesis, University of Heidelberg, January 2010.

[21] ALICE Collaboration, A. Andronic et al., *Transition radiation spectra of electrons from 1-GeV/c to 10-GeV/c in regular and irregular radiators*. Nucl. Instrum. Meth. A558 (2006), 516–525, arXiv:physics/0511229.

[22] Gianbattista-Piero Nicosia, *Stability of the ALICE-HMPID detector in LHC Run 1 and 2 and PID performance in p-Pb collisions at* $\sqrt{s_{NN}}$ *= 8.02 TeV*. Project report, CERN.

[23] Qing Yang et. al., *Measurement of Line-to-Ground Capacitance in Distribution Network Considering Magnetising Impedance Frequency Characteristics*. Article 10.3390/en10040477, Chongqing University, March 2017.

[24] ALICE Collaboration, *ALICE Time Projection Chamber (TPC) - Design and performance*. EPS HEP 2009 128, CERN, July 2009.

[25] Chris Finlay, *Development of the DAQ System for the ALICE TRD*. University of Cape Town, September 2015.

[26] Koos Kortland, *https://docs.hisparc.nl/routenet/en/HiSPARC_ Detector_ Single_ Detector.pdf*, HiSPARC Detector - Single Detector.

[27] Jan-Albert Viljoen, *Detecting Cosmic Ray Trajectories in the Southern Hemisphere using the ALICE TRD*. University of Cape Town, 2016.

[28] ISEG-HV, *https://iseg-hv.com/en/products/detail/NHQ*
Germany.

[29] ALICE CERN, *https://home.cern/science/experiments/alice*

Acknowledgement

Here, I wish to thank all those that helped me during the course of this thesis.

First and foremost, I wish to thank Dr. Thomas Dietel, for his constant motivation, his willingness to always brainstorm and his never ending support and patience. His knowledge and expertise in the field seems endless and I attribute most of my success in this thesis, to him. Thank you for the invitation to join the ALICE team at the University of Cape Town and the opportunity to contribute to the research at ALICE.

To my mom and dad, Nafisa and Babiker, as well as my brothers, Naaga and Kidd, for their continued and endless support throughout the duration of this thesis.

Finally, I wish to thank my brother, Mohamed, thank you for your encouragement and support, your happy outlook on almost everything and your constant reassurances for most of this thesis. You are missed.

Plagiarism Declaration

I know the meaning of plagiarism and declare that all the work in the document, save for that which is properly acknowledged, is my own. This thesis/dissertation has been submitted to the Turnitin module (or equivalent similarity and originality checking software) and I confirm that my supervisor has seen my report and any concerns revealed by such have been resolved with my supervisor.

Signature Removed

Ali Elimam
ELMALI001
January 21, 2021